



HAL
open science

DEM-LBM coupling for partially saturated granular assemblies

N. Younes, Antoine Wautier, R. Wan, O. Millet, F. Nicot, R. Bouchard

► **To cite this version:**

N. Younes, Antoine Wautier, R. Wan, O. Millet, F. Nicot, et al.. DEM-LBM coupling for partially saturated granular assemblies. *Computers and Geotechnics*, 2023, 162, pp.105677. 10.1016/j.compgeo.2023.105677 . hal-04176191

HAL Id: hal-04176191

<https://hal.science/hal-04176191v1>

Submitted on 2 Aug 2023

HAL is a multi-disciplinary open access archive for the deposit and dissemination of scientific research documents, whether they are published or not. The documents may come from teaching and research institutions in France or abroad, or from public or private research centers.

L'archive ouverte pluridisciplinaire **HAL**, est destinée au dépôt et à la diffusion de documents scientifiques de niveau recherche, publiés ou non, émanant des établissements d'enseignement et de recherche français ou étrangers, des laboratoires publics ou privés.

1 DEM-LBM coupling for partially saturated granular
2 assemblies

3 N. Younes^{a,b,c,*}, A. Wautier^b, R. Wan^c, O. Millet^a, F. Nicot^d, R. Bouchard^a

^a*LaSIE, UMR CNRS 7356, University of La Rochelle, La Rochelle, France*

^b*INRAE, Unité de Recherche RECOVER, Aix-en-Provence, France*

^c*Schulich School of Engineering, University of Calgary, Calgary, Canada*

^d*University Savoie Mont Blanc, ISTERre, Chambéry, France*

4 **Abstract**

5 In this paper, we propose a phase-field-based Lattice Boltzmann Method
6 (LBM) model coupled with the Discrete Element Method (DEM) for simu-
7 lating unsaturated granular media over a large range of degrees of saturation.
8 The formation of capillary bridges between grains is computed via an LBM
9 scheme that solves Navier-Stokes and Allen-Cahn equations for multi-phase
10 flow in complex geometries. As for the motions of the grains, these are com-
11 puted within DEM where the contact behavior between spherical particles
12 is based on a simple elastic-plastic contact law. Using an efficient DEM-
13 LBM coupling framework, capillarity effects are explored at the pore scale
14 with the collapse of a sandcastle as a classic illustration. This is done by
15 considering an assembly of several thousands of spherical particles connected
16 by capillary bridges for different degrees of saturation. It is shown that the
17 mean capillary stress increases with the degree of saturation up to a certain
18 threshold beyond which capillary stress drops until complete saturation. In
19 addition, the Soil Water Characteristic Curve is qualitatively recovered and
20 compared to a theoretical model. As such, the proposed DEM-LBM cou-

*Correspondence:
Preprint submitted to *Computers and Geotechnics* (N. Younes)
Email address: nabil.younes@univ-lr.fr (N. Younes)
URL: [orcid.org/ 0000-0003-4431-555X](https://orcid.org/0000-0003-4431-555X) (N. Younes)

21 pling scheme becomes a viable numerical tool that can explicitly model and
22 explore pore-scale phenomena in unsaturated soils.

23 *Keywords:* DEM-LBM coupling, partially saturated medias, capillary
24 cohesion, GPU

25 *PACS:* 0000, 1111

26 *2000 MSC:* 0000, 1111

27 **1. Introduction**

28 The full understanding and modeling of partially saturated granular as-
29 semblies have been a great challenge for both scientists and engineers ([Sheng,](#)
30 [2011](#); [Laloui and Nuth, 2009](#)) over almost a century now. In fact, pore fluid
31 can somehow be seen as a double-edged sword because a small amount of
32 water can only strengthen unsaturated materials until a certain point. As
33 the water content exceeds a certain threshold, capillary bridges merge within
34 the material to lead to a strength reduction and an eventual collapse at high
35 water saturation. This phenomenon is reminiscent of the sandcastle problem
36 that provides a universal example of partially saturated granular material
37 with varying water content.

38 The stress/deformation/failure characteristics of a given soil are usually
39 governed by the effective stress tensor, $\boldsymbol{\sigma}'$, which relates to the transport of
40 forces at the particle contacts within the solid skeleton. The effective stress
41 derives from the celebrated Terzaghi's principle which was first proposed in
42 1925 for fully saturated conditions, and reads in tensorial form as

$$\boldsymbol{\sigma}' = \boldsymbol{\sigma} - u_w \mathbf{I} \quad (1)$$

43 where $\boldsymbol{\sigma}$ is the total stress tensor, u_w is the water pore pressure, and \mathbf{I} is the
 44 identity matrix. It took almost three decades for addressing unsaturated soils
 45 when [Bishop \(1959\)](#) extended Terzaghi’s effective stress principle as follows

$$\boldsymbol{\sigma}' = (\boldsymbol{\sigma} - u_w \mathbf{I}) + \chi(u_a - u_w) \mathbf{I} \quad (2)$$

46 where u_a is the air pressure, u_w the water pressure in capillary bridges, and
 47 χ is some weighting parameter that controls the degree of saturation: $\chi=0$
 48 for dry soils, and $\chi = 1$ for saturated soils, to recover Eq. (1).

49 Previous studies have suggested empirical relations of χ in terms of u_a and
 50 u_w ([Khalili and Khabbaz, 1998](#); [Russell and Khalili, 2006](#)). In addition, arti-
 51 ficial neural networks have been successfully trained to predict the value of χ
 52 ([Lee et al., 2003](#); [Ajdari et al., 2012](#)). Furthermore, other numerical methods
 53 were carried out to estimate χ , for instance, ([Yuan et al., 2018](#); [Liu et al.,](#)
 54 [2020](#)) using 2PFV-DEM and DEM-Fabonnacci-Lattice points discretization,
 55 respectively. Moreover, numerous experimental, analytical, numerical, and
 56 empirical approaches were used to recover the entire Soil-Water Character-
 57 istic Curve (SWCC) ([Fredlund et al., 1997](#); [Deleenne et al., 2015](#); [Fredlund](#)
 58 [and Xing, 1994](#); [Meskini-Vishkaee et al., 2013](#); [Guo et al., 2021](#); [Pedroso and](#)
 59 [Williams, 2011](#); [Li, 2005](#); [Hosseini et al., 2022](#); [Yuan and Chareyre, 2022](#)). In
 60 fact, this is the physics of pore water and air entry and drainage, including
 61 electrochemical effects that control the SWCC. Recently, [Wan et al. \(2019\)](#);
 62 [Pouragha et al. \(2021\)](#) have addressed this issue by using a probabilistic ap-
 63 proach to recover pore size distribution from grain size distribution and the
 64 physics of pore filling or drainage.

65 Several multiscale attempts were performed to determine total and effec-
 66 tive stress tensors within partially saturated granular assemblies using ho-

67 mogenization technique (Wan et al., 2015; Nuth and Laloui, 2008; Vlahinić
68 et al., 2011; Scholtes et al., 2009; Farahnak et al., 2021). It must be noted
69 that most of the works carried out were only applied to low degrees of satura-
70 tion in the pendular regime where only a distinct water bridge exists between
71 a pair of grains.

72 Small granular assemblies (doublets, triplets, and quadruplets) have been
73 frequently investigated in the literature for exploring fundamental proper-
74 ties of capillary bridges (Mielniczuk et al., 2018; Gagneux and Millet, 2014;
75 Benseghier et al., 2020; Miot et al., 2021; Younes et al., 2022; Wang et al.,
76 2017; Di Renzo et al., 2020). Moreover, numerous studies have been con-
77 ducted to understand the behavior of partially saturated media at the scale
78 of a Representative Elementary Volume (REV). For instance, Molecular Dy-
79 namics has been used to model polydispersed particles in 3D conditions to
80 investigate the shear strength of a partially saturated medium (Richefeu
81 et al., 2006). The capillary forces were computed based on the interparti-
82 cle distances separating the grains. In spite of the simplicity of the method,
83 good agreement was found with theoretical experimental data regarding shear
84 strength properties. The same method was also applied by Soulie et al. (2006)
85 to address an axial compression test. Later, Richefeu et al. (2008) carried
86 out 3D-DEM simulations to study shear tests in unsaturated granular media.
87 The capillary forces were taken into account within contacts between spher-
88 ical grains through a contact law supplemented with a capillary force law.
89 This latter is calculated based on an explicit function relating the volume of
90 liquid bridge between a pair of particles to the gap separating them. A good
91 agreement between experimental data and the model was reported in their

92 work.

93 Recently, [Duriez and Wan \(2016\)](#) have modeled unsaturated granular as-
94 semblies using DEM. Capillary bridges were incorporated in DEM calcula-
95 tions by numerically solving the Young-Laplace Equation (YLE) via Finite
96 Differences to compute resulting capillary forces between pairs of grains. The
97 authors highlighted the impact of small degrees of saturation on the mechan-
98 ical response of soil subjected to triaxial tests. It must be noted that in the
99 aforementioned studies, only low degrees of saturation with isolated capillary
100 bridges were investigated because their coalescence could not be handled by
101 none of the numerical methods.

102 To overcome the above-mentioned limitation, several methods were pro-
103 posed by other researchers. For instance, [Delenne et al. \(2013, 2015\)](#) have
104 used 2D Single Component Shan-Chen LBM model along with Molecular Dy-
105 namics to investigate the ensuing apparent cohesive strength for a wide range
106 of degrees of saturation. However, in the latter work, grain particles were
107 fixed, supposing that capillary forces arising from the interstitial fluids are
108 balanced by contact forces between the solid particles. Moreover, it has re-
109 cently been proven in [Benseghier et al. \(2022\)](#) that the numerical constraints
110 proposed by the Shan-Chen LBM model as well as the Carnahan-Starling
111 Equation Of State (EOS) for the temperature are inappropriate. In fact,
112 the latter EOS is thermodynamically consistent only for high temperatures
113 $T > 0.7T_C$ where T_C is defined as the critical temperature¹ which is equal to
114 $T_C = 282.9^\circ\text{C}$, which is non-physical ([Huang et al., 2011, 2015](#)).

¹The critical temperature is a temperature below which a liquid and its vapor coexist.

115 Under fully saturated conditions, [Yang et al. \(2019\)](#) have performed a test
116 case of granular collapse in water using the LBM method coupled with DEM.
117 Furthermore, [Liu et al. \(2020\)](#) have used a model that consists of using DEM
118 coupled with Fabonacci-Point Element discretization of the capillary bridge
119 cap² to compute capillary forces. They were able to model capillary bridges
120 for a wide range of degrees of saturation. Nevertheless, it is important to
121 note that in the latter work, even though high values of degrees of saturation
122 were reported, the coalescence of capillary bridges was not possible.

123 [Melnikov et al. \(2016\)](#) have simulated triaxial tests for mono-dispersed
124 unsaturated media for high values of degrees of saturation using Contact
125 Dynamics (CD) method to model the contacts between spherical grains, cou-
126 pled with a Numerical Energy Minimization (NEM) software for accounting
127 air-water interfaces and the associated capillary forces. They highlighted the
128 impact of air-water capillary interfaces on the mechanical behavior of unsat-
129 urated media subjected to different water contents. However, using the NEM
130 technique, one should select the shape of clusters (trimer, tetrahedral, hep-
131 tamer, pentamer and large) based on defined criteria ([Melnikov et al., 2015](#)).
132 Therefore, re-meshing of clusters must be done once when they change shape.

133 In spite of the numerous studies conducted by many authors, there is
134 still the need for a numerical tool that can model the dynamics of capillary
135 bridges merging or splitting when grains move within a granular assembly at
136 high degrees of saturation.

137 To fill this literature gap, this paper investigates the effect of capillary

²Liquid-solid interface.

138 bridges and the related grain displacements in a partially saturated medium
139 composed of multiple polydispersed solid rigid spherical grains within a dy-
140 namic network topology of capillary bridges where the latter are allowed
141 to merge or split, among others. In particular, the *pendular* and *funicular*
142 regimes will be investigated to demonstrate that capillary forces can give rise
143 to an *apparent cohesion* in a wet granular assembly and to also prove that
144 granular materials become *cohesionless* in the so-called *capillary* regime.

145 With the above-mentioned in mind, we propose a 3D GPU phase-field
146 LBM model to compute the dynamics of capillary bridges and associated
147 forces (Younes et al., 2022). These are then coupled with DEM simula-
148 tions using the software YADE (Šmilauer et al., 2021) which computes the
149 movement of grains under forces that operate between themselves following
150 Newton’s second law of motion. It must be pointed out that a thorough val-
151 idation of the LBM model was conducted by Younes et al. (2022), whereas
152 the code YADE is a reference open-source DEM software.

153 The paper is organized as follows. First, a brief presentation of the phase-
154 field LBM as well as the DEM model used is given. Then, a section is
155 dedicated to the DEM-LBM coupling algorithm, including the synchroniza-
156 tion between the two numerical methods. Finally, the DEM-LBM coupled
157 computation model is used to simulate unsaturated granular assemblies for
158 a large range of saturation in order to determine the evolution of the mean
159 capillary stress and matric suction during crossing the various regimes: from
160 *pendular*, *funicular* to *capillary* regimes.

161 2. Proposed Numerical Models

162 In this paper, the phase-field-based model is adopted where Navier-Stokes
163 Equation (NSE) coupled with Allen-Cahn Equation (ACE) are solved using
164 the Lattice Boltzmann Method. The modeling of partially saturated media as
165 a multiphasic system requires simulating capillary interfaces separating gas
166 from the liquid which are sharp. However, to avoid numerical instabilities, it
167 is preferable to use a regularized interface with a finite width W , as shown
168 in Figure 1(a). A phase field variable $\phi(\xi)$ is conveniently introduced as in
169 Figure 1(b) to determine which is the distinctive phase, whereas within the
170 transition region within W , the phase is rather smooth.

171 In essence, the ACE allows us to compute the evolution of the phase field
172 $\phi(\mathbf{r}, t)$, where \mathbf{r} and t are position and time variables, respectively. Herein,
173 the phase parameter $\phi(\mathbf{r}, t)$ is equal to 1 in the liquid phase, 0 in the gas,
174 and represents the interface for $\phi \in]0; 1[$ as a diffuse interface zone where the
175 two phases coexist. As such, the ACE provides an implicit tracking of the
176 interface which makes it suitable for problems where the interface motion
177 depends on external conditions such as wetting (Liang et al., 2018, 2019;
178 Younes et al., 2022).

179 In this section, the air-water capillary interfaces modeling will be pre-
180 sented. The capillary force computation technique will then be briefly in-
181 troduced; see Younes et al. (2022) for more details, especially the wetting
182 condition. Finally, the Discrete Element Method will also be briefly reviewed
183 for completeness.

184 *2.1. Allen-Cahn and modified Navier-Stokes equations*

185 The time evolution of the phase-field variable, ϕ , which describes the
 186 evolution of the interface is given by the Allen-Cahn Equation

$$\frac{\partial \phi}{\partial t} + \nabla \cdot (\phi \mathbf{u}) = \nabla \cdot [M(\nabla \phi - \lambda \mathbf{n})] \quad (3)$$

187 where \mathbf{u} is the fluid velocity, M the interface mobility, \mathbf{n} the interface unit
 188 normal vector, and λ a parameter related to the interface thickness.

189 Equation (3) is derived from the classical advection equation in which
 190 the velocity is decomposed into two components: (i) advected external fluid
 191 velocity \mathbf{u} , and (ii) the normal interface speed \mathbf{u}_n . The first component is
 192 usually determined from the Navier-Stokes equation, whereas the second,
 193 driven by the thermodynamics constraints, is taken to be proportional to the
 194 interface curvature through mobility such that $\mathbf{u}_n = M\kappa\mathbf{n}$ where κ is the
 195 curvature (Sun and Beckermann, 2007; Chiu and Lin, 2011).

196 In the ACE (3), the unit normal vector to the interface \mathbf{n} as seen in Fig.
 197 1(a) is defined as:

$$\mathbf{n} = \frac{\nabla \phi}{|\nabla \phi|}. \quad (4)$$

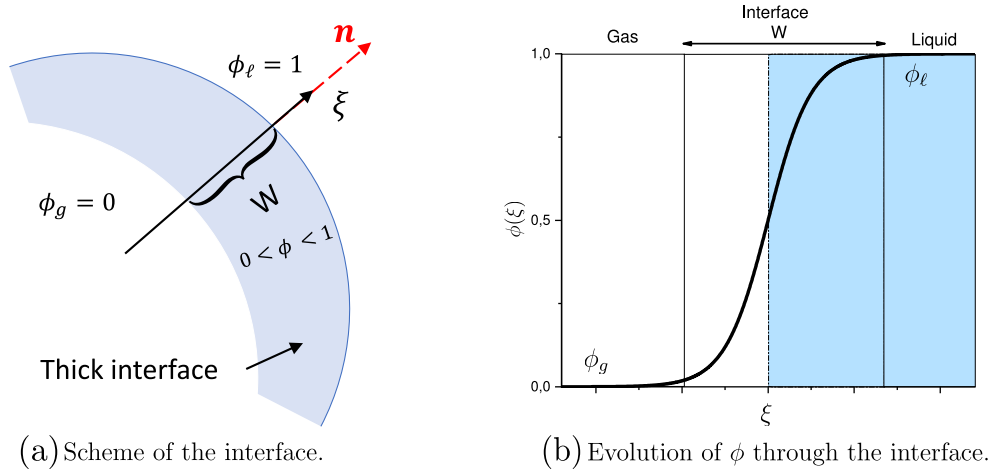


Figure 1: Definition of the regularized interface whose thickness is W and $\phi \in [0; 1]$. The ξ axis is defined as the normal to the interface.

198 Thus, the interface profile at equilibrium, shown in Figure 1(b), is ex-
 199 pressed as

$$\phi^{\text{eq}}(\xi) = \frac{1}{2} \left[1 + \tanh \left(\frac{2\xi}{W} \right) \right] \quad (5)$$

200 where ξ is the local abscissa perpendicular to the interface as shown in Fig-
 201 ure 1(a).

202 The parameter λ is then defined as the derivative of ϕ^{eq} with respect to
 203 ξ , i.e.:

$$\lambda = |\nabla \phi|^{\text{eq}} = \phi_{\xi}^{\text{eq}} = \frac{4\phi(1-\phi)}{W}. \quad (6)$$

204 To consider viscous, immiscible, incompressible two-phase fluid flow, Navier-
 205 Stokes equation is herein augmented with gravitational forces and, most im-
 206 portantly, a surface tension force term \mathbf{F}_s as

$$\rho \left(\frac{\partial \mathbf{u}}{\partial t} + \mathbf{u} \cdot \nabla \mathbf{u} \right) = -\nabla p + \nabla \cdot [\rho \nu (\nabla \mathbf{u} + \nabla \mathbf{u}^T)] + \mathbf{F}_s + \mathbf{B} \quad (7)$$

$$\nabla \cdot \mathbf{u} = 0$$

207 where \mathbf{u} is the fluid velocity, ν is the kinematic viscosity, p is the hydrody-
 208 namic pressure, and \mathbf{B} is the body force.

209 The fluid density field $\rho(\mathbf{r}, t)$ depends on the phase, and hence can be
 210 simply described as a linear interpolation between liquid and gas densities ρ_l
 211 and ρ_g , i.e.

$$\rho(\mathbf{r}, t) = \phi(\rho_l - \rho_g) + \rho_g \quad (8)$$

212 which links Navier-Stokes equation to Allen-Cahn equation.

213 The other parameter coupling ACE to NSE is the surface tension term \mathbf{F}_s
 214 where a potential form is postulated as in [Liang et al. \(2018, 2019\)](#); [Younes](#)
 215 [et al. \(2022\)](#); [Fakhari and Bolster \(2017\)](#), i.e.

$$\mathbf{F}_s = \mu_\phi \nabla \phi \quad (9)$$

216 where μ_ϕ is the chemical potential defined as the minimum of the mixing
 217 energy ([Younes et al., 2022](#); [Penrose and Fife, 1990](#)):

$$\mu_\phi = 4\beta\phi(\phi - 1) \left(\phi - \frac{1}{2} \right) - k\phi''_\xi \quad (10)$$

218 where k and β are constants related to the surface tension γ and the interface
 219 thickness W , i.e.:

$$k = \frac{3}{2}\gamma W; \quad \beta = \frac{12\gamma}{W}. \quad (11)$$

220 It is worth noting that equilibrium is established whenever the chemical po-
 221 tential μ_ϕ vanishes ([Younes et al., 2022](#); [Penrose and Fife, 1990](#)). As such,
 222 ϕ_{eq} can be deduced as the solution of the differential equation (10) with μ_ϕ
 223 equal to zero.

224 *2.2. Associated Lattice Boltzmann models*

225 To solve both Allen-Cahn Equation (3) and Navier-Stokes Equations (7),
 226 the Lattice Boltzmann Method (LBM) is adopted using two Probability Den-
 227 sity Functions (PDFs), $g_\alpha(\mathbf{r}, t)$ and $h_\alpha(\mathbf{r}, t)$ which correspond to ACE and
 228 NSE, respectively. In this work, the Bhatnagar-Gross-Krook (BGK) collision
 229 operator is used (Liang et al., 2018, 2019; Younes et al., 2022) such that

$$g_\alpha(\mathbf{r} + \mathbf{c}_\alpha \Delta t, t + \Delta t) = g_\alpha(\mathbf{r}, t) - \frac{\Delta t}{\tau_g} [g_\alpha(\mathbf{r}, t) - g_\alpha^{eq}(\mathbf{r}, t)] + \Delta t G_\alpha(\mathbf{r}, t) \quad (12)$$

230

$$h_\alpha(\mathbf{r} + \mathbf{c}_\alpha \Delta t, t + \Delta t) = h_\alpha(\mathbf{r}, t) - \frac{\Delta t}{\tau_h} [h_\alpha(\mathbf{r}, t) - h_\alpha^{eq}(\mathbf{r}, t)] + \Delta t H_\alpha(\mathbf{r}, t) \quad (13)$$

231 where τ_g and τ_h are the relaxation times (expressed in lattice units) for $g(\mathbf{r}, t)$
 232 and $h(\mathbf{r}, t)$ probability density functions respectively; G_α and H_α are the
 233 source terms of ACE and NSE, respectively. Finally, \mathbf{c}_α are the discrete
 234 velocities, which depend on the discretization scheme.

235 The main purpose of the LBM is to retrieve the macroscopic variables
 236 based on the PDFs, e.g., the phase-field parameter ϕ , density ρ , and fluid
 237 velocity \mathbf{u} , among others. It turns out that the phase-field parameter ϕ is
 238 given by:

$$\phi = \sum_{\alpha} g_{\alpha}. \quad (14)$$

239 Once ϕ is determined, Eq. (8) is used to calculate the fluid density ρ .
 240 Then, the fluid velocity is calculated as follows:

$$\rho \mathbf{u} = \sum_{\alpha} \mathbf{c}_{\alpha} h_{\alpha} + \frac{\Delta t}{2} (\mu_{\phi} \nabla \phi + \mathbf{B}). \quad (15)$$

241 As for the boundary conditions, a wetting condition is applied to each
 242 particle in order to impose the contact angle θ . The second boundary con-
 243 dition is the classical Bounce-Back condition. Readers can refer to Younes

244 [et al. \(2022\)](#) for more details about the phase-field-based model as well as
 245 the boundary conditions (wetting and bounce-back conditions) used in this
 246 paper.

247 2.3. Numerical calculation of capillary forces

248 As already established in [Younes et al. \(2022\)](#), integrating the appropri-
 249 ate forces exerted by the fluid onto the solid particle leads to the so-called
 250 capillary force. For any capillary bridge shape, the capillary force acting on
 251 a domain Ω is given as

$$\hat{\mathbf{F}}_f = \int_{\Omega} \boldsymbol{\sigma}_f \mathbf{n}_{\Omega} dS + \gamma \int_{\Omega} \mathbf{m} \delta_s(\xi) dS \quad (16)$$

252 where $\boldsymbol{\sigma}_f = -p\mathbf{I} + \boldsymbol{\tau}_{\mu}$ is the fluid stress with \mathbf{I} as the identity tensor, p
 253 is the pressure field, and $\boldsymbol{\tau}_{\mu}$ is the viscous stress tensor, \mathbf{n}_{Ω} is the outward
 254 unit normal vector of the domain Ω , γ is the surface tension, $\delta_s(\xi)$ is the
 255 ‘smooth’ Dirac function of the so-called smooth fluid-fluid interface, and \mathbf{m}
 256 is the tangent vector of the fluid-fluid interface as shown in Figure 2. More
 257 details about the discretization of the Eq. (16) can be found in [Younes et al.](#)
 258 [\(2022\)](#).

259 2.4. Discrete Element Method (DEM)

260 Solid grains are modeled as *rigid* spherical polydispersed particles from the
 261 open-source software YADE based on the Discrete Element Method (DEM)
 262 ([Šmilauer et al., 2021](#)). The method was originally established by [Cundall](#)
 263 [and Strack \(1979\)](#), with particles allowed to overlap at contacts and interact
 264 through contact laws. The elastic-frictional contact law is applied between
 265 overlapping grains. As such, a normal *repulsive* force \mathbf{F}_n is created such that:

$$\|\mathbf{F}_n\| = k_n \delta_n \quad (17)$$

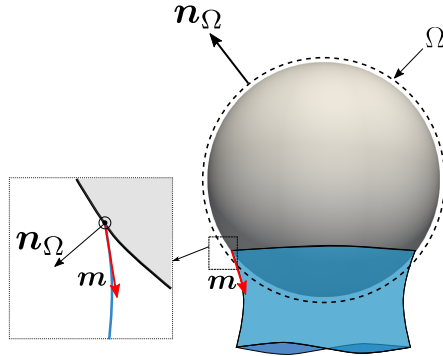


Figure 2: Schematic showing the integration domain Ω , its normal vector pointing outward \mathbf{n}_Ω and the tangent vector to the liquid-gas interface \mathbf{m} .

266 where δ_n is the normal overlapping distance, and k_n is the normal stiff-
 267 ness depending on the radii of particles $R^{(i)}$ and their stiffness E : $k_n =$
 268 $2ER^{(1)}R^{(2)}/(R^{(1)} + R^{(2)})$. Additionally, during overlapping, a tangential force
 269 \mathbf{F}_t is generated which is also proportional to the product of the relative tan-
 270 gential displacement δ_t and the tangential stiffness k_t . The stiffness fraction
 271 α is defined as the ratio of the tangential stiffness to its normal counterpart
 272 ($\alpha = k_t/k_n$). The polydispersed grain parameters of the REV are summa-
 273 rized in Table 1.

Table 1: YADE mechanical parameters for the grains used in Section 4

Parameters	Values	Units
Density ρ_s	2,600	kg.m ⁻³
Stiffness E	110	MPa
Stiffness ratio (α)	0.3	–
Inter-particle friction angle	30	°
$\{D_{\min}; D_{\max}\}$	{80; 108}	μm
Number of particles	3,750	–

274 3. Numerical Procedures

275 The DEM-LBM computations rely on an explicit coupling algorithm whereby
 276 the fluid and solid mechanics simulation modules run sequentially following
 277 a frequency that is modulated by the time scales of the different physics.
 278 Details of the algorithm will be discussed in a later sub-section.

279 We use an in-house LBM master code developed in CUDA C/C++ lan-
 280 guage for GPU computations, whereas the DEM code, YADE, is launched
 281 using a C++ command. The GPU-based code is found to largely alleviate the
 282 computational efforts. A 16GB GPU memory has been used and has been
 283 found to be just adequate for the size of the model herein presented.

284 3.1. Initialization of the grain packing - YADE

285 The initialization of the spherical grains is done in YADE, using the *pack*
 286 package.

287 First, the creation of a cloud of grains as well as the walls on the six sides
 288 of a cubical sample is completed as shown in Figure 3(a). Then, an isotropic

289 confining pressure step is carried out with $\sigma^{\text{conf}} = 100$ kPa by moving the
 290 bounding walls to compress isotropically the granular assembly. Then, the
 291 walls move backward until σ^{conf} reaches 0 kPa as illustrated in Figure 3(b).

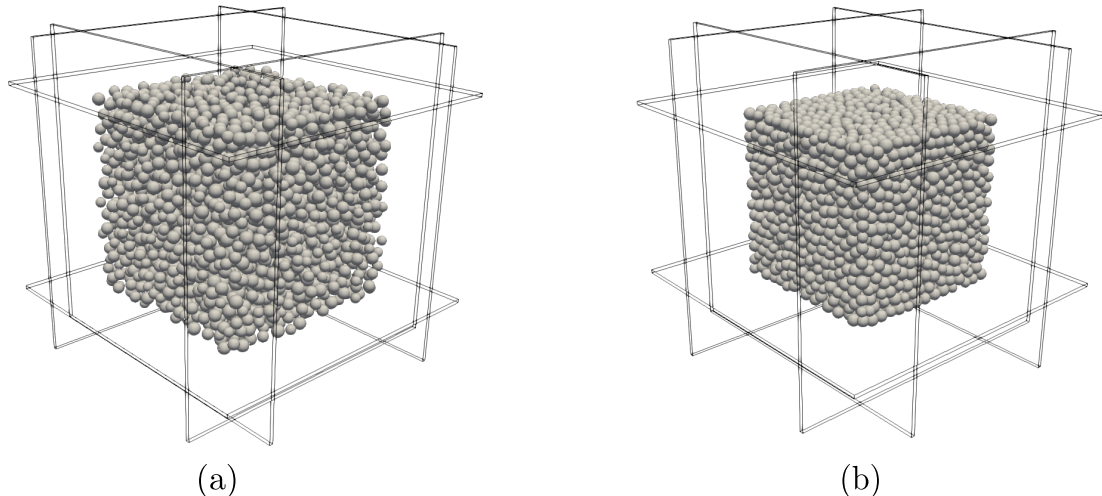


Figure 3: The sequence of steps for generating a polydispersed sample

292 3.2. Initialization of capillary bridges in LBM

293 Capillary bridges are initialized in the form of equally-sized water droplets
 294 between each pair of grains (i, j) for which their separation distance D_{ij} is
 295 less than a user-defined specific value ε as depicted in Figure 4(a). Next,
 296 after running several LBM iterations with fixed grains, the spherical drops
 297 evolve to form capillary bridges of realistic geometries involving more than
 298 a pair of grains; see as seen in Figure 4(b). It is worth mentioning that the
 299 number of LBM iterations to converge to a final liquid geometry depends on
 300 several parameters, e.g. the droplet volume created at mid-distance between
 301 two spherical grains and the value of the surface tension $\tilde{\gamma}$ in lattice units.

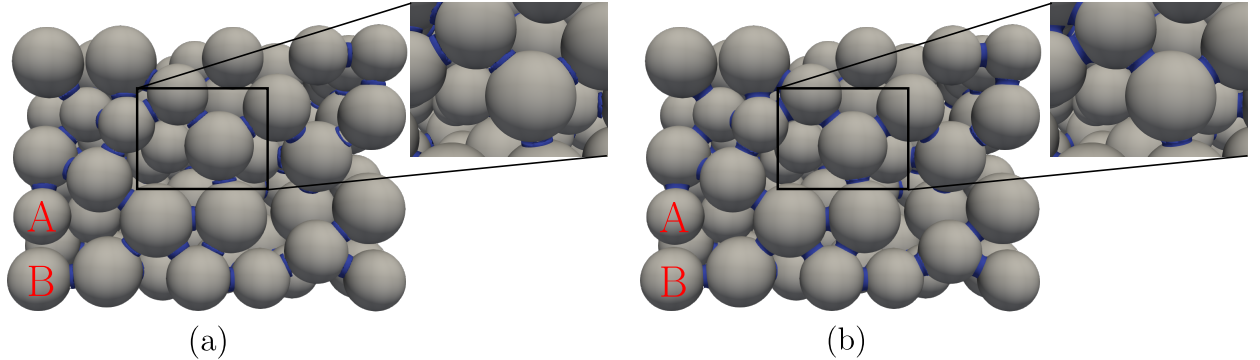


Figure 4: (a) Initialization spherical drops at mid-distance between pair of grains. (b) Converged capillary bridges after several LBM iterations. In (a) the separation distance between particles A and B was larger than the allowed distance ϵ , therefore, no capillary bridge was initialized between these two grains.

302 3.3. DEM-LBM coupling scheme

303 There are two points to be considered in this multiphysics coupling: first,
 304 the time scales involved in the processes are different, and second, the dis-
 305 cretization scheme to solve each piece of physics leads to different time steps.
 306 The latter needs to be synchronized, while also preserving numerical stability
 307 and optimizing computational cost.

308 For numerical stability, the time step Δt_{DEM} in DEM simulations should
 309 be smaller than the critical time step:

$$\Delta t_{\text{crit}} = \min_i \left(R^{(i)} \sqrt{\frac{\rho_s}{E}} \right). \quad (18)$$

310 Regarding the LBM time step, it is usually taken as 1 in lattice units. Us-
 311 ing conversion coefficients as elaborated in [Appendix A.1](#), it can be expressed

312 as:

$$\Delta t_{\text{LBM}} = \sqrt{C_\rho \frac{\tilde{\gamma}}{\gamma} C_L^3}. \quad (19)$$

313 From Eq. (19), it can be seen that once C_L and C_ρ are selected, the
314 only parameter that controls the Δt_{LBM} is the LBM surface tension $\tilde{\gamma}$ in
315 lattice units. Ideally, it is more convenient to maximize Δt_{LBM} for numerical
316 efficiency while also guaranteeing numerical stability. The pros and cons of
317 large values $\tilde{\gamma}$ are discussed in the following.

318 On one hand, the advantages are:

- 319 • Faster simulations:

320 Based on Eq. (15), when $\tilde{\gamma}$ increases, the interface velocity rises.

- 321 • Reasonable relaxation times:

322 Based on Eq. (A.7), when $\tilde{\gamma}$ increases, C_t increases, which makes the
323 relaxation times $\tilde{\tau}_h^{\ell,g}$ larger than $\tilde{\Delta}t/2 = 0.5$ and crucial for numerical
324 stability (Krüger et al., 2017).

325 On the other hand, the disadvantages of large values of $\tilde{\gamma}$ are:

- 326 • Reasonable LBM velocities:

327 According to Krüger et al. (2017), the lattice Mach number should
328 be low ($\text{Ma} \ll 1$). Moreover, LBM fluid velocities are related to $\tilde{\gamma}$.

329 Consequently, the larger the LBM surface tension $\tilde{\gamma}$, the larger the
330 velocities, making the Ma larger which is repugnant when using LBM.

331 One has to consider the above-mentioned points when setting up the value
332 of $\tilde{\gamma}$ to achieve the best computational performance of the coupling, while
333 respecting numerical stability of both LBM and DEM time steps restrictions.

334 Next, to ease the synchronization between these two time steps, the ratio
335 between them must be such that

$$\frac{m}{n} = \frac{\Delta t_{\text{LBM}}}{\Delta t_{\text{DEM}}} \Rightarrow n\Delta t_{\text{LBM}} = m\Delta t_{\text{DEM}} \quad (20)$$

336 where n and m are integers.

337 Figure 5 highlights at which iteration the exchange of data between LBM
338 and DEM takes place. Note that the DEM and LBM algorithms run sequen-
339 tially, hence, during the LBM cycle, the grains are fixed.

340 However, another issue can arise regarding the coupling for two main
341 reasons:

342 • Convergence of spherical droplets to capillary bridges:

343 The capillary bridge is initialized as a spherical drop, and since we
344 focus on the steady state, only the converged capillary bridges are con-
345 sidered³. Thus, 1 single LBM iteration will not be sufficient for the
346 convergence of capillary bridges.

347 • Computational time performance:

348 Data exchange between LBM and YADE is a time-consuming proce-
349 dure. Therefore, making information exchange for every single LBM
350 iteration will drastically reduce the efficiency of the coupling.

351 To overcome this issue, it is convenient to multiply both iteration num-
352 bers (n and m) by a coefficient n_{ratio} , in order: (1) to make the capillary
353 bridge converge to its equilibrium state between two synchronization points,

³The viscous effect is not taken into account in this study. Readers are invited to consult [Younes et al. \(2022\)](#) for more details.

354 and (2) to avoid huge computation time in exchanging data between LBM
 355 and YADE. Therefore, DEM and LBM numbers of iterations needed for the
 356 simulations are:

$$N_{\text{LBM}} = n_{\text{ratio}} \times n \tag{21}$$

$$N_{\text{DEM}} = n_{\text{ratio}} \times m.$$

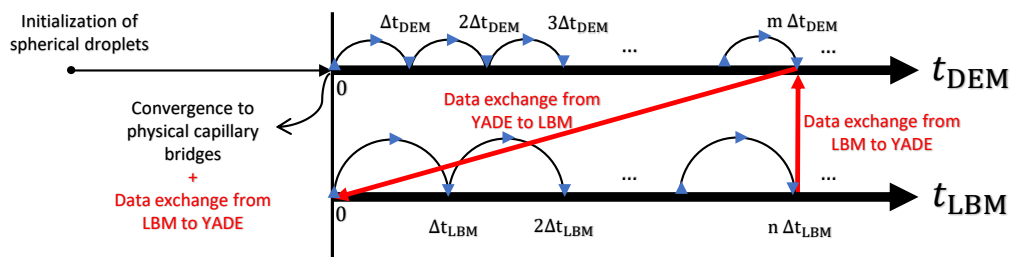


Figure 5: Timelines of both LBM and DEM simulations and information exchange procedure between LBM code and YADE

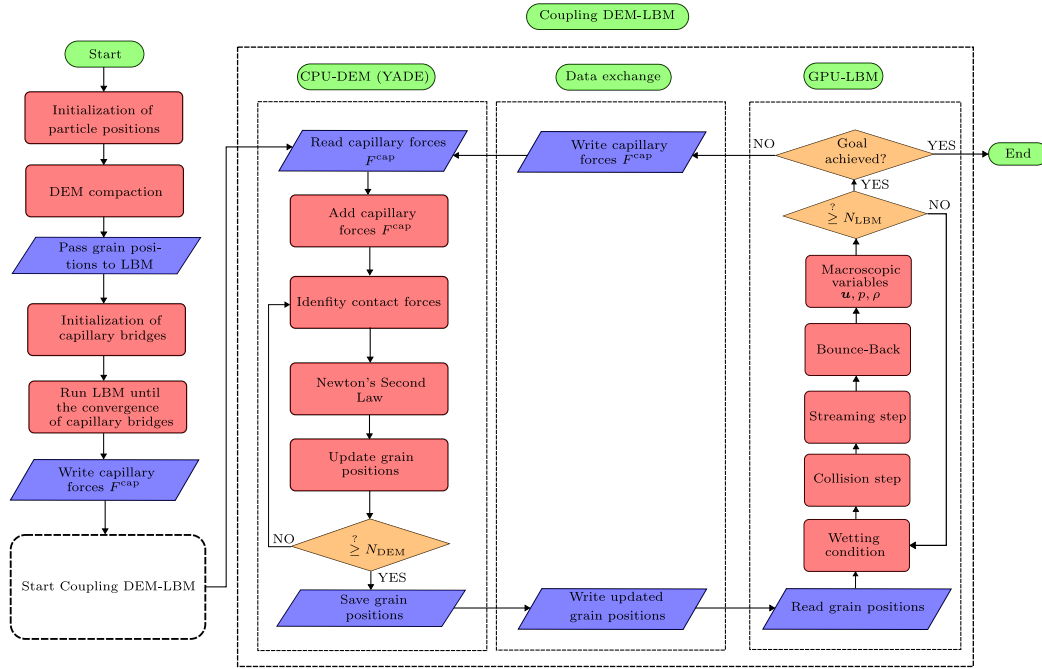


Figure 6: Flowchart showing the coupling between LB and DE methods

357 Figure 6 presents the flowchart of the coupling between LBM and DEM.
 358 The first steps correspond to the initialization of a cloud of particles in YADE
 359 to be then passed to LBM in order to initialize spherical drops at the mid-
 360 distance of the grains. Next, multiple LBM iterations will be run until the
 361 convergence of all capillary bridges. Capillary forces are then computed and
 362 used in YADE to couple the DEM-LBM calculations.

363 The main steps of the DEM are herein summarized: (a) contact forces
 364 are determined, (b) Newton's Second Law is applied for each grain to update
 365 the velocities of the grains, and (c) particle positions are updated. Then, if
 366 the DEM iteration is less than N_{DEM} , the DEM algorithm will return back
 367 to step (a). Otherwise, the new positions of particles are saved.

368 Finally, the updated grain positions are used to start the LBM algorithm.
369 The main steps in the LBM algorithm include: (1) wetting condition, (2)
370 collision, (3) streaming, (4) Bounce-Back boundary condition, and (5) deter-
371 mination of macroscopic variables. Then, the synchronization condition is
372 verified. If the number of iterations is less than N_{LBM} , the cycle will return
373 to step (1). Otherwise, capillary forces F^{cap} are computed for each grain.
374 Next, capillary forces are read in YADE and applied to grains and back and
375 forth iteratively.

376 As mentioned far back in the introduction, the LBM and DEM models
377 have been separately validated. Then, the only validation concerns the cou-
378 pling of the two models which is rather challenging, given the scale of the
379 problem. Experimental results that explore the small scale in relation to the
380 dynamics of particles and the associated topology of liquid bridges are scarce,
381 and very difficult to realize.

382 In what follows in the paper, we will be conducting an *indirect* validation
383 of the coupling aspect by investigating the capillary stress versus water satu-
384 ration relationship in an assembly of wetted particles. The numerical results
385 show a departure from Bishop’s relationship, which is validated by available
386 data in the literature.

387 **4. Application to capillary water in a granular assembly**

388 In this section, we apply the DEM-LBM coupling model to simulate the
389 mechanical behavior of a granular assembly composed of 3,750 spherical
390 grains following a uniform grain size distribution such that $D_{\text{max}}/D_{\text{min}} = 1.35$
391 with $D_{\text{max}} = 108 \mu\text{m}$, and $D_{\text{min}} = 80 \mu\text{m}$. The DEM parameters were sum-

392 marized in Table 1.

393 One may ask whether the number of grains (3,750) is sufficient to justify
394 the requirements of a Representative Elementary Volume (REV). It turns
395 out that for such a narrow grain size distribution where the grain diameters
396 are limited, the chosen number of grains is deemed large enough for an REV
397 at least in the dry and low saturation conditions. When the water cluster
398 dimensions approach the sample dimension the concept of REV becomes
399 more questionable, but this question is far beyond the scope of the paper.

400 The LBM domain size is $N_x \times N_y \times N_z = 350 \times 350 \times 350$, with a mesh size
401 of $\Delta x = 5 \times 10^{-6}$ m, and an imposed contact angle of $\theta = 25^\circ$ as a boundary
402 condition that remains constant throughout the entire simulation (Younes
403 et al., 2022). The air-water capillary interfaces are modeled with a surface
404 tension $\gamma = 0.072$ N.m⁻¹. The critical time step based on Eq. (18) is $\Delta t_{\text{crit}} =$
405 1.944×10^{-7} s. The selected value of LBM surface tension is $\tilde{\gamma} = 10$. Using
406 Eq. (19), the LBM time step is $\Delta t_{\text{LBM}} = 1.3176 \times 10^{-7}$ s. Therefore, the DEM
407 time step Δt_{DEM} is chosen equal to LBM time step ($n = m = 1$ from Section
408 3.3) along with $n_{\text{ratio}} = 50$, and the ratio between DEM time step and the
409 critical one is $\Delta t_{\text{DEM}}/\Delta t_{\text{crit}} = 0.6774$ which is reasonably high for not slowing
410 down DEM simulations significantly. Accordingly, the relaxation times of
411 water and air are $\tilde{\tau}_h^\ell = 0.5158$ and $\tilde{\tau}_h^g = 0.7846$, respectively⁴ (in lattice
412 units). Both relaxation times are larger than 0.5, which ensures numerical
413 stability (Krüger et al., 2017).

414 From a mechanical point of view, and according to Scholtès et al. (2009);

⁴Water and air viscosities are $\nu^{\text{water}} = 10^{-6}$ m².s⁻¹ and $\nu^{\text{air}} = 1.8 \times 10^{-5}$ m².s⁻¹, respectively, at a temperature of $T = 20^\circ\text{C}$.

415 Scholtes et al. (2009); Duriez and Wan (2016, 2017); Duriez et al. (2017),
 416 the total stress tensor $\boldsymbol{\sigma}^{\text{tot}}$ can be decomposed into the sum of the so-called
 417 contact stress tensor $\boldsymbol{\sigma}^{\text{cont}}$ that accounts for grain-to-grain interactions and
 418 the capillary stress tensor $\boldsymbol{\sigma}^{\text{cap}}$ to take into account the effect of capillary
 419 bridges:

$$\boldsymbol{\sigma}^{\text{tot}} = \boldsymbol{\sigma}^{\text{cap}} + \boldsymbol{\sigma}^{\text{cont}} \quad (22)$$

420 In the framework of micro-mechanics, the contact stress tensor is calculated
 421 via the Love-Weber stress tensor formula $\boldsymbol{\sigma}^{\text{LW}}$ expressed as follows (Love,
 422 2013; Weber, 1966; Nicot et al., 2013; Duriez and Wan, 2016, 2017; Duriez
 423 et al., 2017)

$$\boldsymbol{\sigma}^{\text{cont}} = \boldsymbol{\sigma}^{\text{LW}} = \frac{1}{V} \sum_c \mathbf{f}_{ij}^c \otimes \boldsymbol{\ell}_{ij}^c \quad (23)$$

424 where \mathbf{f}_{ij}^c is the contact force between pair of grains (i and j) and $\boldsymbol{\ell}_{ij}^c$ is
 425 the branch vector from the center of i to that of j , and \otimes refers to dyadic
 426 product.

427 Previously, in Scholtès et al. (2009); Scholtes et al. (2009); Duriez and
 428 Wan (2016, 2017); Duriez et al. (2017) the capillary stress $\boldsymbol{\sigma}^{\text{cap}}$ has been
 429 computed directly based on capillary forces using a Love-Weber-like expres-
 430 sion. However, this relation between capillary forces and capillary stresses
 431 applies exclusively to the *pendular* regime where isolated capillary bridges
 432 only exist between pairs of particles.

433 In this work, the involved degree of saturation range extends the *pendular*
 434 regime into the *funicular* and the *capillary* ones as the isolated liquid bridges
 435 coalesce, making it complicated to calculate the capillary stress using the

436 virial of force theorem⁵. Instead, we herein compute capillary stresses σ^{cap}
437 indirectly using Eq. (22), i.e.:

$$\sigma^{\text{cap}} = \sigma^{\text{tot}} - \sigma^{\text{cont}}. \quad (24)$$

438 As a matter of fact, it is possible to compute the capillary stress tensor as
439 reconstructed from the topology of the liquid phase in the pores, including the
440 distribution of wetted grain surfaces and air-water, air, solid-water interfaces
441 as derived in Duriez et al. (2017); but this is outside the scope of this work.

442 4.1. Dry sample

443 Firstly, the sample is initialized as shown in Figure 7(a) and the lateral
444 walls are then removed. As there is no capillary water within the sample,
445 the latter readily collapses to form a pile of grains after a few seconds as
446 illustrated in Figure 7(b). The angle of repose of the pile approaches the
447 macroscopic friction angle of the sample (Al-Hashemi and Al-Amoudi, 2018).

448 As the sample is dry, the capillary stress is necessarily zero. Moreover,
449 the computed mean contact stress⁶ also gives an extremely low value of ap-
450 proximately -0.46 Pa (here negative means compression), corresponding to
451 self-weight of the pile. Therefore, based on Eq. (22), the total stress tensor
452 is also approximately zero.

453 4.2. Wet sample

454 Next, the same sample as in Figure 7(a) is considered, but under unsat-
455 urated conditions. Contrary to Figure 7(b), Figure 8(b) shows that despite

⁵This theorem consists in replacing contact forces in Eq. (23) by capillary forces.

⁶Mean contact stress is defined as $\frac{1}{3}\text{Tr}(\sigma^{\text{cont}})$

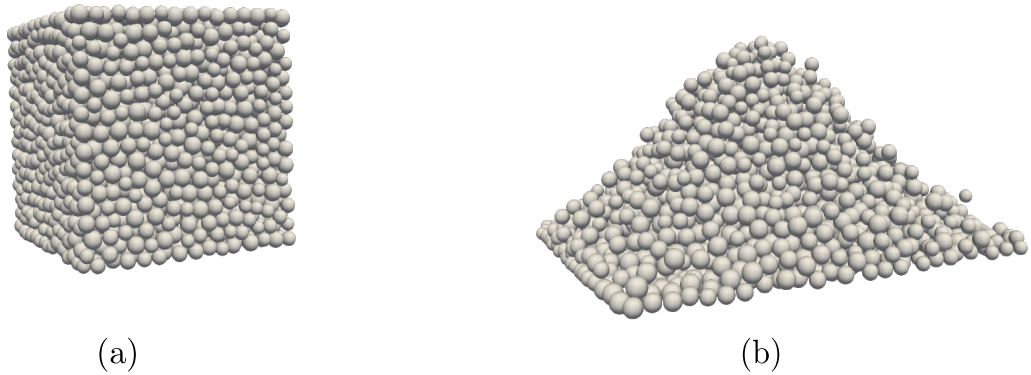


Figure 7: (a) Initial configuration of the dry sample confined within a box of 6 walls. (b) Collapse of the dry sample when lateral walls are removed.

456 removing the lateral walls, the partially saturated specimen ($S_r \approx 54\%$) does
 457 not collapse, thanks to capillary forces just like in the case of a self-standing
 458 wet sandcastle at the beach. Figure 8(b) readily demonstrates the capillary
 459 effects at hand.

460 4.2.1. Initial degree of saturation setup

461 It is certainly of interest to numerically investigate the effects of capillarity
 462 at different degrees of saturation. This is, in our numerical experiment, we
 463 initialize the granular assembly starting with a known volume of water as per
 464 the procedure outlined in Section 3.2, and let the system reach equilibrium
 465 both hydraulically and mechanically under zero external stress through many
 466 cycles of coupled DEM-LBM computations.

467 A total number of 10,877 spherical droplets are initialized between par-
 468 ticles at a cutoff distance of $\varepsilon = 5\ \mu\text{m}$ which corresponds to approximately

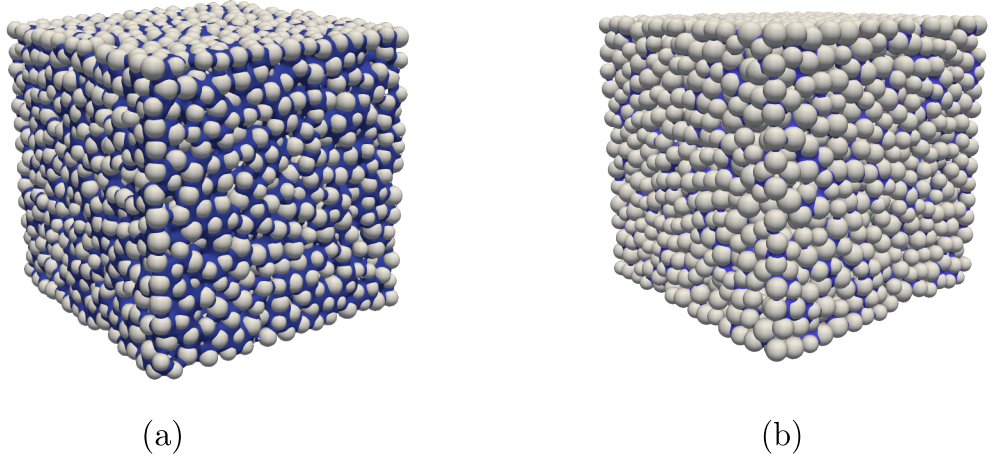


Figure 8: (a) Initial configuration of a wet cubical sample confined within six walls. (b) Stable wet sample even after removing the lateral walls. The degree of saturation in this example is $S_r \approx 54\%$.

469 10% of the maximum particle radius in the assembly. It is worth noting that
 470 several simulations were carried out for different values of ε , and it has been
 471 found that the results are not influenced by ε . Also, by growing or reduc-
 472 ing the size of the initialized spherical droplet radius we thereby control the
 473 increase or decrease of the degree of saturation in our numerical exercise.

474 Finally, a variety of interesting results will next be explored to establish
 475 how both matric suction s and the capillary stress tensor evolve as a function
 476 of the degree of saturation.

477 4.2.2. *Matric suction and Soil Water Characteristic Curve*

478 For a given initial volume of water in the granular sample, we can readily
 479 calculate the degree of saturation as well as the volumetric water content,

480 knowing the porosity. On the other hand, determining the suction operating
 481 at the sample level is more complicated, but can be estimated as the aver-
 482 age of all local suctions s^i at capillary menisci weighted by their respective
 483 volumes as in [Deleenne et al. \(2015\)](#), i.e.

$$s = \frac{1}{V_w} \sum_{i=1}^{N^{\text{cap}}} \overbrace{(u_a - u_w^i)}^{s^i} V_w^i \quad (25)$$

484 where V_w is the total water volume, N^{cap} is the number of capillary bridges,
 485 u_w^i is the pore water pressure within the i^{th} capillary bridge, and V_w^i is the
 486 volume of the i^{th} capillary bridge. Here, the air pressure u_a is negligible when
 487 compared to the negative water pressure u_w within the capillary bridges so
 488 that suction takes on a positive value.

489 Figure 9 shows the evolution of suction as computed from Eq. (25) when
 490 the sample is wetted at various degrees of saturations (S_r on the left y-axis)
 491 or volumetric water contents⁷ (θ_w on the right y-axis).

492 For low degrees of saturation which correspond to the *pendular* regime,
 493 the suction s is high, roughly equal to 13 kPa. As the degree of saturation
 494 increases, the suction drops drastically to reach a limiting value of $s \approx 4$
 495 kPa for $S_r \in [15; 70]$ %. Thereafter, S_r reaches nearly $S_r \approx 70$ % when a
 496 change in slope is observed at which point suction will tend to 0 as the level
 497 of saturation is being further increased.

498 The above description of the curve is essentially the so-called Soil Water
 499 Characteristic Curve (SWCC) which defines the water retention property of

⁷The volumetric water content is defined as follows: $\theta_w = \phi^p S_r$ where ϕ^p is the sample porosity.

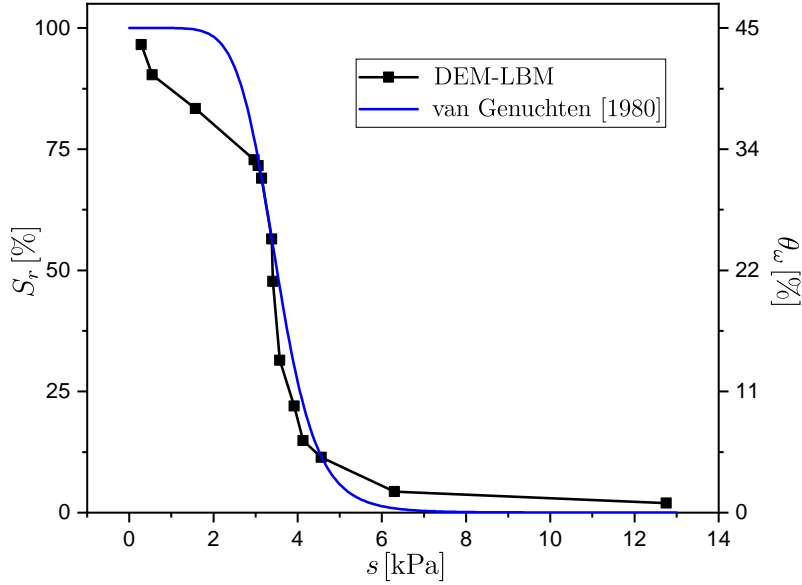


Figure 9: Degree of saturation and volumetric water content evolution in terms of the matric suction s of the present model. [Van Genuchten \(1980\)](#) model has been plotted for comparison.

500 unsaturated soils. For comparison purposes, the numerical simulation data
 501 has been fitted with the well-known Van Genuchten model given by

$$S_r = \left[\frac{1}{1 + (\alpha s)^n} \right]^m \quad (26)$$

502 where n [-] is the parameter responsible for the soil size distribution, m [-] is
 503 related to the symmetry of the retention curve, and α [kPa⁻¹] is the inverse
 504 of the suction at the Air Entry Value (AEV) ([Matlan et al., 2014b](#); [Oh and
 505 Lu, 2014](#); [Matlan et al., 2014a](#); [Fredlund and Xing, 1994](#)).

506 The van Genuchten fitting parameters are found to be $n = 7$, $m = 1.2302$,
 507 and $\alpha = 0.2739$ with the corresponding best fitted curve shown in Figure 9.
 508 Based on the statistical study reported in [Matlan et al. \(2014a\)](#) the values of

509 α range between -0.445 and 1.5020 kPa^{-1} and those of n between 1.472 and
510 9.731 [-] for sandy soils. Interestingly, the van Genuchten parameters that fit
511 our numerical SWCC fall within the range of sandy soils as a check for its
512 consistency.

513 Recently, [Hosseini et al. \(2021\)](#) have studied the effect of porosity on the
514 SWCC. According to their findings, as the porosity increases, m increases
515 as well. For porosities within the range of 0.4 and 0.5 , the corresponding
516 m values fall between 0.75 and 1.66 . Therefore, the value of $m = 1.2302$
517 obtained in our numerical simulations is also totally reasonable with the
518 numerical sample porosity being equal to 0.44 . It must be noted that for
519 a saturation degree larger than 70% , our numerical findings deviate from
520 the van Genuchten model. This non-smoothness behavior is probably the
521 consequence of the dynamics of the air invading the water phase in the pores,
522 thus creating large changes in the water menisci topology. It is essential
523 to highlight that this non-smooth behavior likely arises from the dynamic
524 interaction between air invading into the water phase within the pores. As
525 a consequence, significant changes occur in the topology of water menisci.
526 This observation aligns with the experimental results of [Matlan et al. \(2014b\)](#)
527 regarding sandy soils which is indeed our case here— $D_{\min} = 80 \mu\text{m} > 50 \mu\text{m}$
528 ([Das, 2019](#)).

529 The findings of this numerical experiment indicate that the proposed
530 DEM-LBM model is capable of capturing one of the main features in un-
531 saturated soils, i.e., the development of matric suction s and its variation
532 with water saturation. In order to further evaluate the DEM-LBM model,
533 the distinctive properties of the capillary stress tensor σ^{cap} will be next in-

534 vestigated.

535 4.2.3. Capillary stress tensor $\boldsymbol{\sigma}^{\text{cap}}$

536 In the absence of the lateral walls with a total stress tensor $\boldsymbol{\sigma}^{\text{tot}}$ being
537 sensibly zero, the capillary stress still subsists following Eq. (22), i.e.:

$$\boldsymbol{\sigma}^{\text{tot}} = \boldsymbol{\sigma}^{\text{cap}} + \boldsymbol{\sigma}^{\text{cont}} = \mathbf{0} \xrightarrow{\boldsymbol{\sigma}^{\text{tot}} \approx \mathbf{0}} \boldsymbol{\sigma}^{\text{cap}} = -\boldsymbol{\sigma}^{\text{cont}} \neq \mathbf{0}. \quad (27)$$

538 Since capillary forces are attractive in nature, they will tend to bring the
539 particles closer to interpenetrate further, which will induce new repulsive
540 forces. The particles then move such that an equilibrium state is finally
541 reached when repulsive forces and attractive capillary forces are equal. Thus,
542 the liquid bridge being in tension by virtue of surface tension forces, the effect
543 of capillarity is tensile.

544 The following analyses will be based on the mean capillary stress⁸ $\boldsymbol{\sigma}^{\text{cap}}$
545 defined as:

$$p^{\text{cap}} = \frac{1}{3} \text{Tr}(\boldsymbol{\sigma}^{\text{cap}}). \quad (28)$$

546 The computations in the DEM code YADE follow the continuum mechan-
547 ics convention where compression is negative and tension is positive. Accord-
548 ingly, a positive p^{cap} corresponds to the traction that confers the sample with
549 an *apparent cohesion* under unconfined conditions.

550 Figure 10(a) shows the evolution of the mean capillary stress with time
551 until equilibrium is reached for different degrees of saturation. From a compu-

⁸Although not necessarily true in the most general case, the computed capillary stress tensor $\boldsymbol{\sigma}^{\text{cap}}$ turned out to be nearly spherical (with $\sigma_{xx} \approx \sigma_{yy} \approx \sigma_{zz}$) due to the initial arrangement of the solid particles and liquid bridges, cf. [Appendix B](#).

552 tational viewpoint and for a given saturation, capillary forces f_{cap} calculated
553 from the topology of the capillary bridges from the LBM side enter the DEM
554 calculations in YADE as attractive forces. These, when applied to the par-
555 ticles, will make them become closer and overlap so that repulsive contact
556 forces set up. The search for an equilibrium state, both mechanically and
557 hydraulically, eventually leads to the plateau shown in Figure 10(a). The
558 coupling between DEM-LBM calculations were described in detail in Section
559 3.3.

560 Generally speaking, the higher the degree of saturation with more liquid
561 bridges pulling the grains together, the higher p^{cap} as well as the plateau.
562 However, it can be observed from Figure 10(a) that the mean capillary stress
563 value at the equilibrium state initially increases with the degree of saturation
564 up to a certain value of $S_r = 67.47\%$, after which there is a drop for $S_r =$
565 72.77% . This indicates that there must be a maximum value of p^{cap} for the
566 range of S_r between 11.41% and 72.77% .

567 As a comparative note, the phenomenon of increased capillary stress can
568 also be observed within a small granular assembly composed of three grains
569 (Gagneux and Millet, 2016). Under such condition, it was found that the
570 capillary force will increase significantly (about 30%) when capillary bridges
571 merge to become one cluster, whereas they were three isolated capillary
572 bridges before.

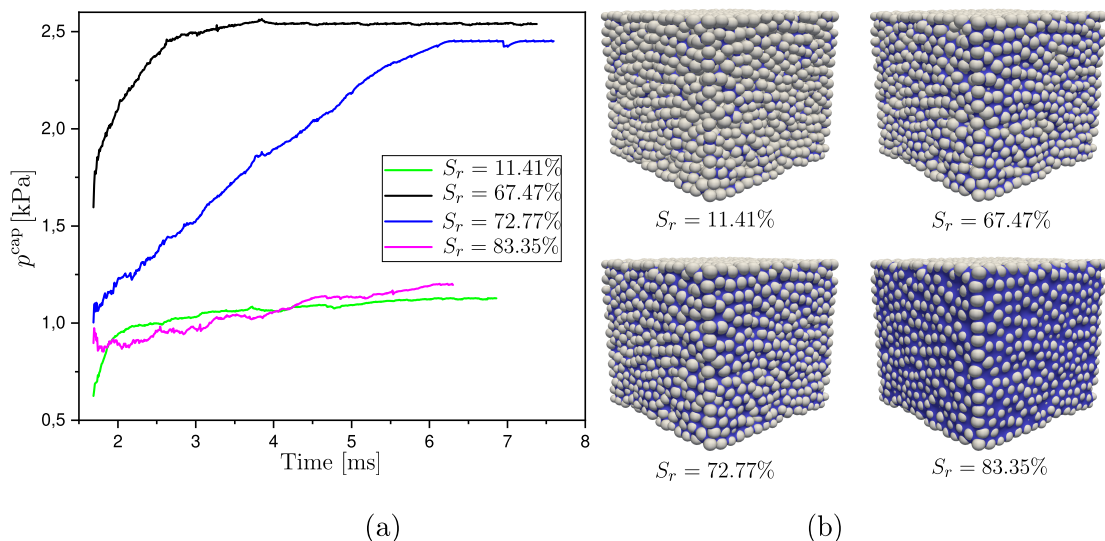


Figure 10: (a) The evolution of mean capillary stress p^{cap} [kPa] over time in DEM-LBM coupled simulations for selected values of degrees of saturation are shown, (b) Snapshots of the partially saturated samples at equilibrium for different values of $S_r \in \{11.41; 67.47; 72.77; 83.35\}$ %.

573 We next explore the evolution of p^{cap} as well as that of s in terms of
574 degree of saturation and volumetric water content θ_w as plotted on the same
575 Figure 11(a). To explain the evolution of p^{cap} and s , a *topology* analysis
576 of capillary bridges and air bubbles is necessary. To avoid ambiguities, the
577 displayed numbering of labeled⁹ air bubbles and capillary bridges, as shown
578 in Figures 11(b) and (c), respectively, is explained next. For example, for a
579 degree of saturation $S_r = 11.41\%$, the total number of capillary bridges is

⁹The Flood-Fill algorithm is used to detect capillary bridges as well as air bubbles. Every air bubble and capillary bridge is labeled and given an ID as indicated in Figure 11(b) and (c) for air bubbles and capillary bridges, respectively.

580 2,088 and it would be impossible to display them all labeled with distinct
581 colors. We, therefore, show only the first 6 labeled ID's as cut-off value so
582 that capillary bridges ID's higher up to 2,088 are represented by the same
583 color (orange). The same labeling and coloring scheme is applied to air
584 bubbles in Figure 11(b).

585 Turning to point (1) which corresponds to $S_r = 11.41 \%$, it can be seen
586 that the wet granular assembly contains an extensive network of air clus-
587 ters together with a large number of capillary bridges as illustrated in Fig-
588 ures 11(b) and (c), respectively.

589 As the degree of saturation increases and reaches point (2) which corre-
590 sponds to the peak of p^{cap} ($S_r \approx 68 \%$), the isolated capillary bridges develop
591 into one big cluster, with plenty of trapped air bubbles within the capillary
592 bridge cluster. This particular point corresponds to the maximum curvature
593 in the SWCC where the suction s starts to decrease, as seen in Figure 11(a).

594 It is important to note that the granular system has only one large cluster
595 of capillary bridges from step (2) onward. For higher degrees of saturation
596 at (3) and (4), the originally continuous air phase dwindles with ubiquitous
597 trapped air bubbles, thus resulting in concurrent drops in suction and mean
598 capillary stress.

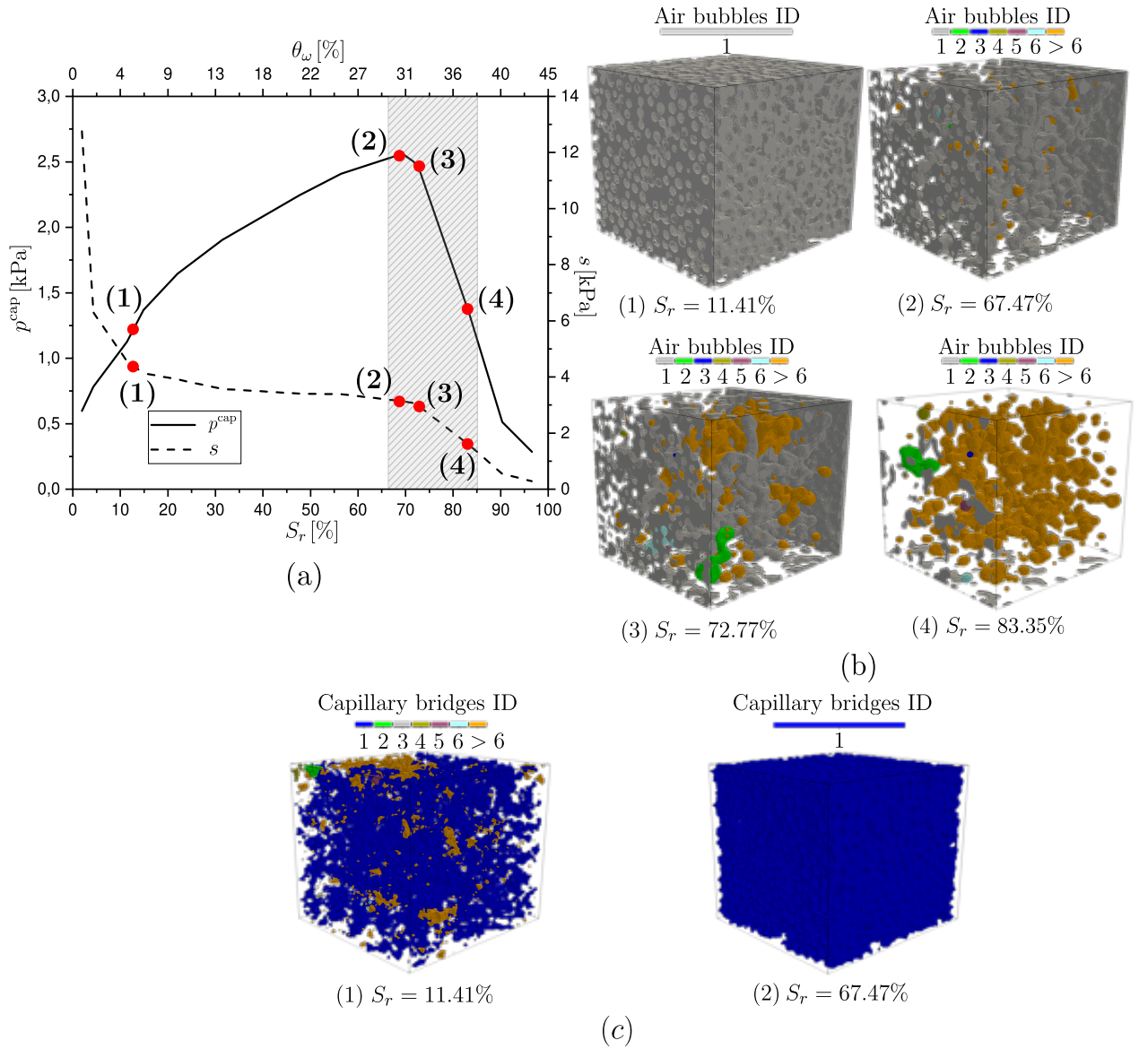


Figure 11: Mean capillary stress p^{cap} [kPa] based on Eq. (27) and suction s [kPa] in terms of degrees of saturation S_r and volumetric water content θ_ω at the bottom and top x-axis, respectively. (b) Snapshots of the distribution of air bubbles within the domain as the system is wetted for 4 different degrees of saturation $S_r \in \{11.41; 67.47; 72.77; 83.35\}$ %. (c) Snapshots of capillary bridges within the granular media for 2 different degrees of saturation $S_r \in \{11.41; 67.47\}$ %.

599 These two aforementioned steps (3 & 4), in fact, correspond to the stage
 600 of AEV in SWCC for a path starting from a high saturation. The AEV stage
 601 occurs when the air starts filling the voids of the granular system. In order
 602 to provide a clearer picture, Figure 12 shows snapshots of a section taken in
 603 the middle of the specimen at various levels of saturation similar to those
 604 shown in Figure 11(b).

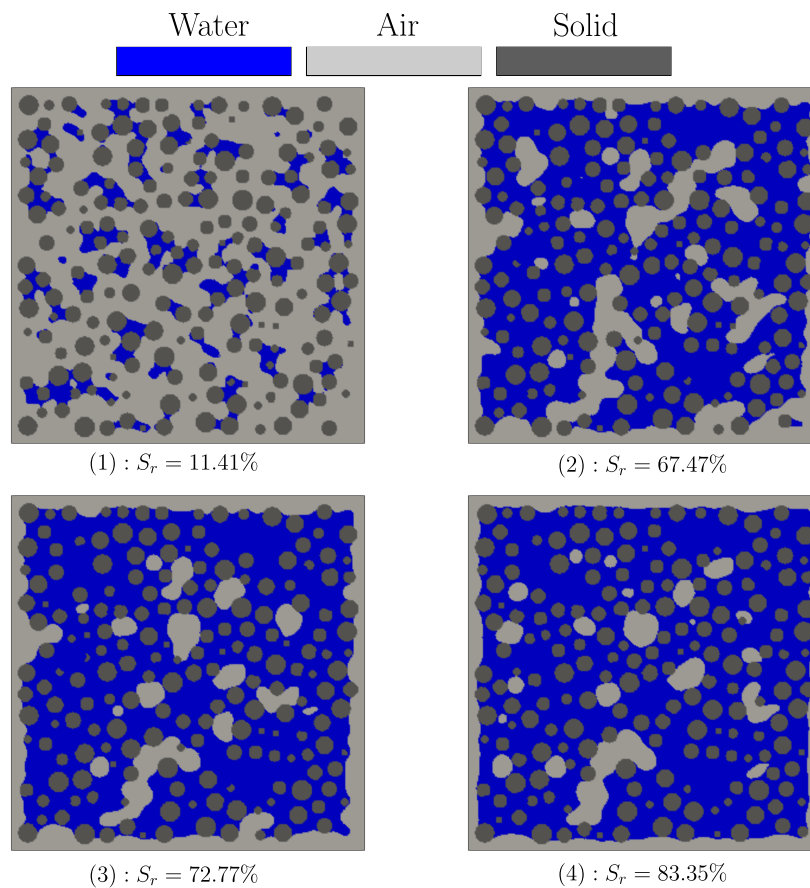


Figure 12: Snapshots of a section made in the middle of the sample at various degrees of saturation. Blue, gray, and dark gray colors correspond to water, air, and solid grains, respectively.

605 As can be seen, for high degrees of saturation, the sample contains one
606 extensively large interconnected water cluster engulfing isolated trapped air
607 bubbles which correspond to the *capillary*¹⁰ regime, as shown in (4) at $S_r =$
608 83.35%. As the degree of saturation decreases, the air starts to infiltrate
609 through the specimen to become partially connected to the external air, as
610 seen in (3) and (2). These two latter configurations represent the *funicular*
611 regime. Lastly, for low degrees of saturation below (1): isolated and coalesced
612 capillary bridges can be found, and the air becomes one big interconnected
613 cluster which corresponds to the end of the *pendular* regime or the beginning
614 of the *funicular* regime.

615 4.2.4. Capillary stress tensor and Bishop's equation

616 In light of the DEM-LBM simulations, it is tempting to revisit current
617 issues in unsaturated soil mechanics such as how the stresses are partitioned
618 to reflect the contribution of each of the phases. The existence of a single
619 effective stress which controls both skeleton deformation and failure of un-
620 saturated soils is herein not addressed as it has been thoroughly discussed
621 in Duriez et al. (2018); Nuth and Laloui (2008); Laloui and Nuth (2009);
622 Scholtes et al. (2009); Vlahinić et al. (2011). However, the capillary stress
623 tensor will be analyzed to elucidate Bishop's stress equation.

624 As seen before, the capillary stress tensor is spherical, hence, the relation

¹⁰The degree of saturation marking the onset of the capillary regime depends on the water spatial distribution in the sample. In laboratory experiments, air invades the pores from the sample boundaries. In this case, the capillary regime is likely to be observed for a wider range of saturation.

625 between the capillary stress tensor $\boldsymbol{\sigma}^{\text{cap}}$ and the suction s as a scalar can be
626 simplified (Duriez et al., 2017) as such:

$$\boldsymbol{\sigma}^{\text{cap}} = sS_r\mathbf{I}. \quad (29)$$

627 In fact, Eq. (29) represents a simplified version of Bishop's equation pre-
628 viously seen in Eq. (2) with the assumption that $\chi = S_r$, which is debatable
629 and subject of controversy in the literature. On the other hand, in our DEM-
630 LBM computations, the capillary stress tensor can certainly be deduced by
631 simple subtraction of the contact stress tensor from the total stress one fol-
632 lowing Eq. (27).

633 Figure 13 gives the plot of p^{cap} as calculated from simplified Bishop's
634 equation (Eq. (29)) and our DEM-LBM simulations (Eq. (27)) in terms of
635 degrees of saturation S_r and volumetric water content θ_ω on the bottom and
636 top x-axis of the figure, respectively.

637 As the granular assembly is being wetted, both mean capillary stresses
638 will increase until a certain threshold ($S_r \approx 68\%$, $\theta_\omega \approx 30\%$) is reached
639 beyond which the specimen starts to lose the effects of capillarity. We can
640 observe that p^{cap} based on Bishop's simplified equation is always less than
641 our computed values.

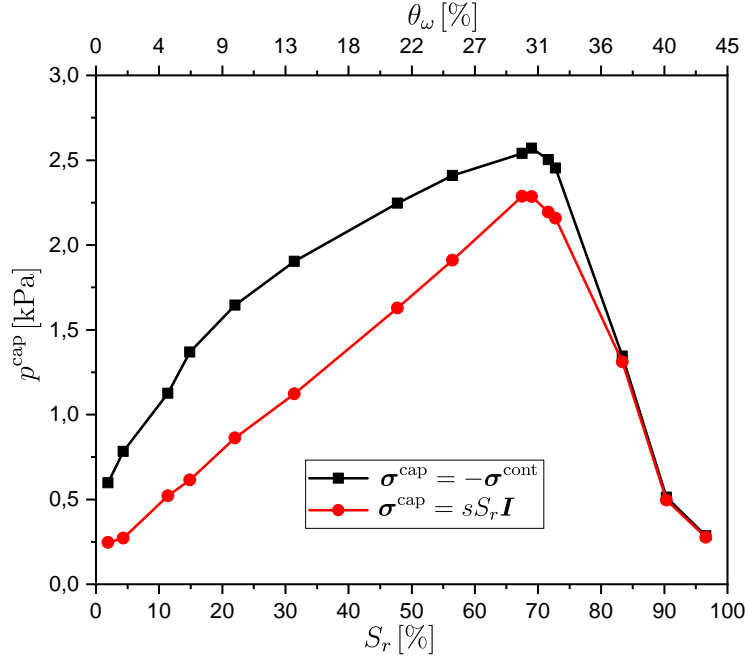


Figure 13: Mean capillary stresses p^{cap} [kPa] based on Eqs. (27) and (29) evolution in terms of degrees of saturation S_r [%] and volumetric water contents θ_ω [%].

642 Despite the same tendency displayed in both curves, they do not perfectly
643 match, especially before the threshold is reached. The reason for this lies in
644 the assumption: $\chi = S_r$ noted earlier in Bishop's equation.

645 To investigate whether S_r and χ coincide or not, χ is back-calculated from
646 our DEM-LBM computations for various degrees of saturation and suction
647 values. Here, since the specimen is unconfined ($\boldsymbol{\sigma}^{\text{tot}} = \mathbf{0}$), the capillary stress
648 coincides with the negative of the contact stress tensor, and thus:

$$\chi = \frac{1}{3} \frac{\text{Tr}(\boldsymbol{\sigma}^{\text{cont}})}{s}. \quad (30)$$

649 Several points should be noted:

- 650 • The effective stress parameter χ can be generally defined as a tensor,
651 but since in our work, all the stress tensors are diagonal and isotropic,
652 mean values are considered, *i.e.*, $\frac{1}{3}\text{Tr}(\boldsymbol{\sigma})$;
- 653 • Eq. (30) is deduced from Eq. (2) which is formulated in the Soil Me-
654 chanics convention (compression > 0 and tension < 0). The mean
655 contact stress is therefore positive, $\frac{1}{3}\text{Tr}(\boldsymbol{\sigma}^{\text{cont}}) > 0$;
- 656 • The air pressure u_a is negligible with respect to the mean capillary
657 stress.

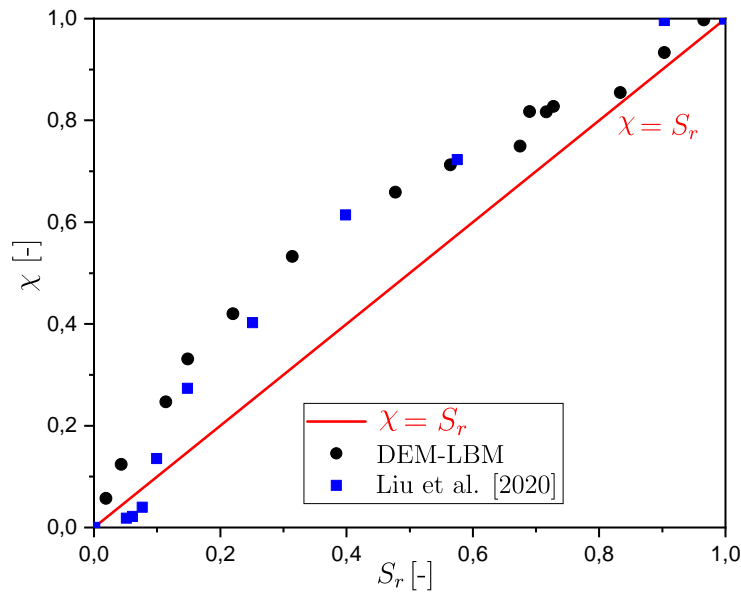


Figure 14: The evolution of χ in terms of S_r . Linear relation ($\chi = S_r$) and Liu et al. (2020) results are plotted for comparison.

658 The back-calculated χ is then plotted against S_r as shown in Figure 14
659 where χ and S_r almost never coincide proving why both σ^{cap} are not exactly
660 similar in Figure 13. To insure that our findings are right on course, another
661 numerical data set for χ in terms of S_r (Liu et al., 2020) has been added to
662 Figure 14.

663 Our findings and the ones determined by Liu et al. (2020) are generally in
664 good agreement. Clearly, the two numerical results do not line up perfectly,
665 especially for low levels of degrees of saturation $S_r < 10\%$. For this particular
666 range, and contrary to our findings, Liu et al. (2020) have found that $\chi < S_r$.

667 The above discrepancy can be attributed to the difference between particle
668 size distributions used in this work and theirs. In fact, the grain size used
669 in Liu et al. (2020) is roughly four times smaller than the one we have used
670 in this study, which results in changes not only in porosity but also the
671 attendant capillary effects—the smaller the particles, the greater the capillary
672 effect. Moreover, and according to Bishop and Blight (1963), for clayey
673 soils the effective stress parameter χ is smaller than the S_r not only for low
674 saturation but even up to approximately 50% (Talybont Clay). In contrast,
675 silty-sandy soils lead to $\chi < S_r$ only for low degrees of saturation $S_r < 20$
676 %—see Vaich moraine soil in Bishop and Blight (1963). Hence, χ tends to
677 remain greater than S_r as particle size increases, which renders our results
678 reasonable since our particle size is greater than the one used in Liu et al.
679 (2020).

680 5. Conclusion

681 In this work, a DEM-LBM algorithm is developed in order to investi-
682 gate the characteristics—dynamics of liquid bridges and capillarity effects—
683 of partially saturated granular assemblies over a large range of degrees of
684 saturation S_r . Regarding the Lattice Boltzmann Method (LBM), a GPU
685 phase-field-based model is adopted to solve both Allen-Cahn and Navier-
686 Stokes equations to capture the presence of capillary interfaces between liquid
687 and gas phases. As such, the proposed LBM approach successfully handles
688 the dynamics of isolated as well as coalesced capillary bridges, and most
689 importantly calculates capillary forces throughout *pendular*, *funicular* and
690 *capillary* regimes.

691 Concerning the Discrete Element Method (DEM), the open-source YADE
692 is used, accounting for contacts between rigid spherical grains. The key point
693 of the coupling between the two methods lies in the judicious integration of
694 capillary forces computed via LBM into the DEM calculation cycles.

695 The predictive capabilities of the DEM-LBM algorithm are investigated
696 in the modeling of unsaturated granular assemblies. First, the variation of
697 suction in terms of the degree of saturation or volumetric water content has
698 been qualitatively recovered and compared to van Genuchten model.

699 Furthermore, when the sample is wetted at various degrees of saturation,
700 we recover the classic result of a self-standing sandcastle under no confine-
701 ment, whereas an unconfined cubical dry sample readily collapses. Another
702 finding is the elucidation of the mean capillary stress for several degrees of
703 saturation. The obtained results demonstrate that the mean capillary stress
704 only increases with the degree of saturation up to a certain level $\approx 68\%$ after

705 which there is a drop, explainable by the dynamics of water clusters filling the
706 void space. Next, we also have convincingly demonstrated that the so-called
707 Bishop’s parameter χ does not coincide with the degree of saturation S_r , but
708 takes a form that can be readily calculated numerically and that coincides
709 with experimental results.

710 To conclude, the DEM-LBM coupling seems to be a viable tool to study
711 partially saturated media over different regimes—*pendular*, *funicular*, and
712 *capillary*, traversing the different transitions in a continuous manner and
713 elucidating the dynamics of the different phases at the pore scale. Further
714 studies should address the micro-mechanical behavior of partially saturated
715 granular assemblies when subjected to drying/wetting cycles to investigate
716 *in extenso* the merging of capillary bridges with hysteretic phenomena and
717 their influence on the capillary mean stress.

718 **Acknowledgements**

719 The authors would like to express their sincere gratitude to the Nouvelle-
720 Aquitaine Region for funding the StabDigue project, to the IRN Geomech
721 network for facilitating valuable discussions, and to the French National Cen-
722 tre for Space Studies (CNES) for having supported this work.

723 **CRedit authorship contribution statement**

724 **N. Younes:** Software, Validation, Formal analysis, Writing – original
725 draft, Writing – review & editing, Visualization, Methodology, Investiga-
726 tion. **A. Wautier:** Conceptualization, Investigation, Review & editing,
727 Supervision, Funding acquisition. **R. Wan:** Conceptualization, Writing –

728 review & editing, Supervision, Funding acquisition, Project administration.
 729 **O.Millet:** Conceptualization, Review & editing, Supervision, Project ad-
 730 ministration, Funding acquisition. **F. Nicot:** Conceptualization, Review &
 731 editing, Supervision. **R. Bouchard:** Writing – original draft, Visualization.

732 **Appendix A. LBM parameters**

733 *Appendix A.1. Conversion units coefficients*

734 In LBM simulations, the mesh size and the time step are supposed to be
 735 equal to 1 in lattice units (lu) to ease numerical implementation. Therefore,
 736 a rescaling between physical and lattice units must be established to make
 737 the simulations consistent with the physics, because all the LBM parameters
 738 are given in lu.

739 For the sake of simplicity, the following convention will be used: all the
 740 parameters represented with a tilde $\widetilde{\square}$ are expressed in lattice units¹¹ ‘lu’,
 741 and without the tilde represents the physical units¹² \square . For instance, $\widetilde{\Delta x} = 1$
 742 lu and $\Delta x = 1 \mu\text{m}$.

Solving ACE and NSE equations with LBM involves the use of only three physical units; length, time and mass. Therefore, the conversion between lattice and physical units can be derived from the re-scaling of lengths, time, and densities defined as follows

$$\Delta x = C_L \underbrace{\widetilde{\Delta x}}_{=1} \quad \Delta t = C_t \underbrace{\widetilde{\Delta t}}_{=1} \quad \rho = C_\rho \widetilde{\rho} \quad (\text{A.1})$$

¹¹The lattice unit ‘lu’ will be omitted in the rest of the paper.

¹²All the of the physical parameter values will be written with their associated units.

743 where the units involved are respectively meters (m), seconds (s), and kilo-
744 gram per cubic meter kg/m^3 . Eq. (A.1) gives the so-called canonical con-
745 version factors. The first step to determine the conversion coefficient of any
746 given physical parameter is to link its unit to the three canonical factors. For
747 instance, the dimensional analysis of the surface tension γ gives:

$$[\gamma] = \text{N} \cdot \text{m}^{-1} = \overbrace{\text{kg} \cdot \text{m} \cdot \text{s}^{-2}}^{\text{N}} \cdot \text{m}^{-1} = \frac{\text{kg}}{\text{m}^3} \cdot \text{m}^3 \cdot \text{s}^{-2}. \quad (\text{A.2})$$

748 Thus, the conversion between surface tension γ in lattice and physical units
749 yields to:

$$C_\gamma = \frac{\gamma}{\tilde{\gamma}} = C_\rho \frac{C_L^3}{C_t^2}. \quad (\text{A.3})$$

750 If one is interested in computing the physical time step within an LBM
751 simulation Δt , he should calculate it using Eq. (A.3) as follows:

$$C_t = \frac{\Delta t}{\tilde{\Delta t}} = \sqrt{C_\rho C_\gamma C_L^3}. \quad (\text{A.4})$$

752 Therefore, once the mesh size Δx and C_ρ are fixed¹³, the only parameter
753 that controls the time step is $\tilde{\gamma}$. Similarly, force conversion unit $C_F = \frac{F}{\tilde{F}}$ is
754 computed based on dimensional analysis:

$$[F] = \text{N} = \text{kg} \cdot \text{m} \cdot \text{s}^{-2} = C_\rho \frac{C_L^4}{C_t^2}. \quad (\text{A.5})$$

755 From Eq. (A.5), the force conversion coefficient expresses:

$$C_F = \frac{F}{\tilde{F}} = C_\rho \frac{C_L^4}{C_t^2}. \quad (\text{A.6})$$

¹³Usually, for the sake of simplicity, the conversion factor of density is unity $C_\rho = 1$

756 *Appendix A.2. Choice of LBM parameters*

757 In order to accurately model real multiphase fluids, one should choose
 758 wisely his simulation parameters, especially in LBM models.

759 First, the interface width is selected, generally $\widetilde{W} = 5 - 10$ lu to make
 760 the interface smooth enough—as shown in Fig. A.15—to preclude numerical
 761 instabilities .

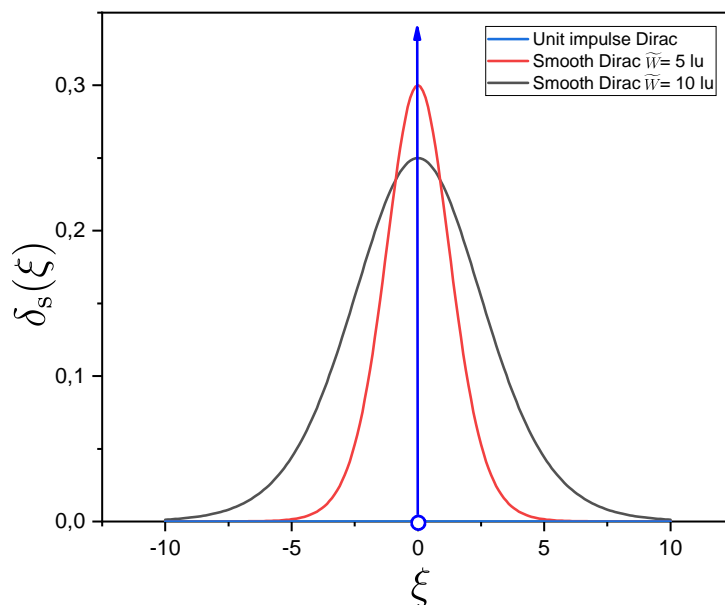


Figure A.15: Smooth Dirac functions for $\widetilde{W} \in \{5; 10\}$ lu as well as the unit impulse Dirac function.

762 Next, densities $\tilde{\rho}_l$ and $\tilde{\rho}_g$ are calculated using Eq. (A.1). As previously
 763 mentioned, C_ρ is usually taken as 1 which is the case in all the simulations
 764 in this paper. Afterwards, C_L is calculated based on the physical and LBM

765 characteristic lengths L_c and \tilde{L}_c as follows: $C_L = \frac{L_c}{\tilde{L}_c}$. Following that, $\tilde{\gamma}$ is
766 chosen whereby C_t is calculated using Eq. (A.4). Once the C_t is determined,
767 the relaxation times $\tilde{\tau}_h^\ell$ and $\tilde{\tau}_h^g$ are computed based on the scaling of the
768 liquid and gas viscosities:

$$\nu^{\ell,g} = \underbrace{\tilde{c}_s^2 \left(\tilde{\tau}_h^{\ell,g} - \frac{\tilde{\Delta t}}{2} \right)}_{\tilde{\nu}^{\ell,g}} \overbrace{\frac{C_L^2}{C_t}}^{C_\nu} \iff \tilde{\tau}_h^{\ell,g} = \frac{C_t \nu^{\ell,g}}{\tilde{c}_s^2 C_L^2} + \frac{\tilde{\Delta t}}{2}. \quad (\text{A.7})$$

769 According to Krüger et al. (2017), numerical instabilities are observed if
770 the values of $\tilde{\tau}_h^{\ell,g}$ are too close of $\frac{1}{2}$. Moreover, $\tilde{\gamma}$ determines C_t whereby
771 relaxation times are calculated.

772 Appendix B. Capillary stress tensor characteristics

773 It can be seen from Figure B.16 that only the diagonal terms are different
774 than zero and roughly equal ≈ 1.12 kPa, and the non-diagonal terms are
775 nearly zero $\approx 7.21 \times 10^{-4}$ kPa. The largest difference between the diagonal
776 terms is 0.15% which is negligible.

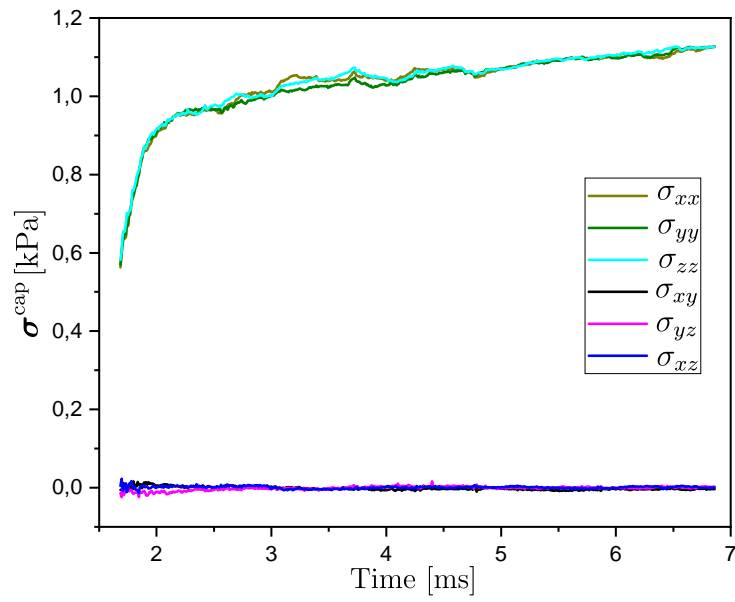


Figure B.16: Capillary stress tensor components $(\sigma_{xx}, \sigma_{yy}, \sigma_{zz}, \sigma_{xy}, \sigma_{yz}, \sigma_{xz})$ evolution in time for $S_r = 11.41\%$.

777 **References**

- 778 Ajdari, M., Habibagahi, G., Ghahramani, A., 2012. Predicting effective stress
779 parameter of unsaturated soils using neural networks. *Computers and*
780 *Geotechnics* 40, 89–96.
- 781 Al-Hashemi, H.M.B., Al-Amoudi, O.S.B., 2018. A review on the angle of
782 repose of granular materials. *Powder technology* 330, 397–417.
- 783 Benseghier, Z., Cuéllar, P., Luu, L.H., Delenne, J.Y., Bonelli, S., Philippe,
784 P., 2020. Relevance of free jet model for soil erosion by impinging jets.
785 *Journal of Hydraulic Engineering* 146, 04019047.
- 786 Benseghier, Z., Millet, O., Philippe, P., Wautier, A., Younes, N., Liberge,
787 E., 2022. Relevance of capillary interfaces simulation with the shan–chen
788 multiphase lb model. *Granular Matter* 24, 1–18.
- 789 Bishop, A.W., 1959. The principle of effective stress. *Teknisk ukeblad* 39,
790 859–863.
- 791 Bishop, A.W., Blight, G., 1963. Some aspects of effective stress in saturated
792 and partly saturated soils. *Geotechnique* 13, 177–197.
- 793 Chiu, P.H., Lin, Y.T., 2011. A conservative phase field method for solving
794 incompressible two-phase flows. *Journal of Computational Physics* 230,
795 185–204.
- 796 Cundall, P.A., Strack, O.D., 1979. A discrete numerical model for granular
797 assemblies. *geotechnique* 29, 47–65.
- 798 Das, B.M., 2019. *Advanced soil mechanics*. CRC press.

- 799 Delenne, J.Y., Richefeu, V., Radjai, F., 2013. Capillary states of granular
800 materials in the funicular state, in: AIP Conference Proceedings, American
801 Institute of Physics. pp. 1023–1026.
- 802 Delenne, J.Y., Richefeu, V., Radjai, F., 2015. Liquid clustering and capillary
803 pressure in granular media. *Journal of Fluid Mechanics* 762.
- 804 Di Renzo, A., Picarelli, G., Di Maio, F.P., 2020. Numerical investigation of
805 funicular liquid bridge interactions between spherical particles. *Chemical
806 Engineering & Technology* 43, 830–837.
- 807 Duriez, J., Eghbalian, M., Wan, R., Darve, F., 2017. The micromechanical
808 nature of stresses in triphasic granular media with interfaces. *Journal of
809 the Mechanics and Physics of Solids* 99, 495–511.
- 810 Duriez, J., Wan, R., 2016. Stress in wet granular media with interfaces via
811 homogenization and discrete element approaches. *Journal of Engineering
812 Mechanics-ASCE* 142.
- 813 Duriez, J., Wan, R., 2017. Contact angle mechanical influence in wet granular
814 soils. *Acta Geotechnica* 12, 67–83.
- 815 Duriez, J., Wan, R., Pouragha, M., Darve, F., 2018. Revisiting the existence
816 of an effective stress for wet granular soils with micromechanics. *International
817 Journal for Numerical and Analytical Methods in Geomechanics* 42,
818 959–978.
- 819 Fakhari, A., Bolster, D., 2017. Diffuse interface modeling of three-phase
820 contact line dynamics on curved boundaries: A lattice boltzmann model

821 for large density and viscosity ratios. *Journal of Computational Physics*
822 334, 620–638.

823 Farahnak, M., Wan, R., Pouragha, M., Eghbalian, M., Nicot, F., Darve, F.,
824 2021. Micromechanical description of adsorptive-capillary stress in wet
825 fine-grained media. *Computers and Geotechnics* 137, 104047.

826 Fredlund, D.G., Xing, A., 1994. Equations for the soil-water characteristic
827 curve. *Canadian geotechnical journal* 31, 521–532.

828 Fredlund, M.D., Fredlund, D.G., Wilson, G., 1997. Prediction of the soil-
829 water characteristic curve from grain-size distribution and volume-mass
830 properties, in: *Proc., 3rd Brazilian Symp. on Unsaturated Soils, Rio de*
831 *Janeiro*. pp. 13–23.

832 Gagneux, G., Millet, O., 2014. Analytic calculation of capillary bridge prop-
833 erties deduced as an inverse problem from experimental data. *Transport*
834 *in Porous Media* 105, 117–139.

835 Gagneux, G., Millet, O., 2016. An analytical framework for evaluating the
836 cohesion effects of coalescence between capillary bridges. *Granular matter*
837 18, 1–13.

838 Guo, L., Chen, G., Li, C., Xia, M., Gong, S., Zheng, L., 2021. A bound water
839 model for numerical simulation of swcc in the wide suction range based on
840 dda. *Computers and Geotechnics* 139, 104378.

841 Hosseini, R., Kumar, K., Delenne, J.Y., 2021. Investigating the effect of
842 porosity on the soil water retention curve using the multiphase lattice
843 boltzmann method, in: *EPJ Web of Conferences, EDP Sciences*. p. 09007.

- 844 Hosseini, R., Kumar, K., Delenne, J.Y., 2022. Investigating the source of
845 hysteresis in the soil-water characteristic curve using the multiphase lattice
846 boltzmann method. arXiv preprint arXiv:2204.07174 .
- 847 Huang, H., Krafczyk, M., Lu, X., 2011. Forcing term in single-phase
848 and shan-chen-type multiphase lattice boltzmann models. Phys. Rev. E
849 84, 046710. URL: [https://link.aps.org/doi/10.1103/PhysRevE.84.](https://link.aps.org/doi/10.1103/PhysRevE.84.046710)
850 [046710](https://link.aps.org/doi/10.1103/PhysRevE.84.046710), doi:10.1103/PhysRevE.84.046710.
- 851 Huang, H., Sukop, M., Lu, X., 2015. Multiphase lattice boltzmann methods:
852 Theory and application .
- 853 Khalili, N., Khabbaz, M., 1998. A unique relationship for χ for the de-
854 termination of the shear strength of unsaturated soils. Geotechnique 48,
855 681–687.
- 856 Krüger, T., Kusumaatmaja, H., Kuzmin, A., Shardt, O., Silva, G., Viggien,
857 E.M., 2017. The lattice boltzmann method. Springer International Pub-
858 lishing 10, 4–15.
- 859 Laloui, L., Nuth, M., 2009. On the use of the generalised effective stress in the
860 constitutive modelling of unsaturated soils. Computers and Geotechnics
861 36, 20–23.
- 862 Lee, S., Lee, S.R., Kim, Y., 2003. An approach to estimate unsaturated
863 shear strength using artificial neural network and hyperbolic formulation.
864 Computers and Geotechnics 30, 489–503.
- 865 Li, X., 2005. Modelling of hysteresis response for arbitrary wetting/drying
866 paths. Computers and Geotechnics 32, 133–137.

- 867 Liang, H., Liu, H., Chai, Z., Shi, B., 2019. Lattice boltzmann method for
868 contact-line motion of binary fluids with high density ratio. *Phys. Rev. E*
869 99, 063306.
- 870 Liang, H., Xu, J., Chen, J., Wang, H., Chai, Z., Shi, B., 2018. Phase-field-
871 based lattice boltzmann modeling of large-density-ratio two-phase flows.
872 *Phys. Rev. E* 97, 033309.
- 873 Liu, X., Zhou, A., Shen, S.I., Li, J., Sheng, D., 2020. A micro-mechanical
874 model for unsaturated soils based on dem. *Computer Methods in Applied*
875 *Mechanics and Engineering* 368, 113183.
- 876 Love, A.E.H., 2013. *A treatise on the mathematical theory of elasticity.*
877 Cambridge university press.
- 878 Matlan, S., Mukhlisin, M., Taha, M., 2014a. Statistical assessment of models
879 for determination of soil–water characteristic curves of sand soils. *Interna-*
880 *tional Journal of Geological and Environmental Engineering* 8, 797–802.
- 881 Matlan, S.J., Mukhlisin, M., Taha, M.R., 2014b. Performance evaluation of
882 four-parameter models of the soil-water characteristic curve. *The Scientific*
883 *World Journal* 2014.
- 884 Melnikov, K., Mani, R., Wittel, F.K., Thielmann, M., Herrmann, H.J., 2015.
885 Grain-scale modeling of arbitrary fluid saturation in random packings.
886 *Physical Review E* 92, 022206.
- 887 Melnikov, K., Wittel, F.K., Herrmann, H.J., 2016. Micro-mechanical failure
888 analysis of wet granular matter. *Acta Geotechnica* 11, 539–548.

- 889 Meskini-Vishkaee, F., Mohammadi, M., Vanclooster, M., 2013. A scaling
890 approach, predicting the continuous form of soil moisture characteristics
891 curve, from soil particle size distribution and bulk density data. *Hydrology
892 & Earth System Sciences Discussions* 10.
- 893 Mielniczuk, B., Millet, O., Gagneux, G., El Youssoufi, M.S., 2018. Char-
894 acterisation of pendular capillary bridges derived from experimental data
895 using inverse problem method. *Granular Matter* 20, 1–11.
- 896 Miot, M., Veylon, G., Wautier, A., Philippe, P., Nicot, F., Jamin, F., 2021.
897 Numerical analysis of capillary bridges and coalescence in a triplet of
898 spheres. *Granular Matter* 23, 1–18.
- 899 Nicot, F., Hadda, N., Guessasma, M., Fortin, J., Millet, O., 2013. On the
900 definition of the stress tensor in granular media. *International Journal of
901 Solids and Structures* 50, 2508–2517.
- 902 Nuth, M., Laloui, L., 2008. Effective stress concept in unsaturated soils:
903 Clarification and validation of a unified framework. *International journal
904 for numerical and analytical methods in Geomechanics* 32, 771–801.
- 905 Oh, S., Lu, N., 2014. Uniqueness of the suction stress characteristic curve
906 under different confining stress conditions. *Vadose Zone Journal* 13.
- 907 Pedroso, D.M., Williams, D.J., 2011. Automatic calibration of soil–water
908 characteristic curves using genetic algorithms. *Computers and Geotechnics*
909 38, 330–340.

- 910 Penrose, O., Fife, P.C., 1990. Thermodynamically consistent models of phase-
911 field type for the kinetic of phase transitions. *Physica D: Nonlinear Phe-*
912 *nomena* 43, 44–62.
- 913 Pouragha, M., Eghbalian, M., Wan, R., Wong, T., 2021. Derivation of soil
914 water retention curve incorporating electrochemical effects. *Acta Geotech-*
915 *nica* 16, 1147–1160.
- 916 Richefeu, V., El Youssoufi, M.S., Peyroux, R., Radjai, F., 2008. A model
917 of capillary cohesion for numerical simulations of 3d polydisperse granular
918 media. *International Journal for Numerical and Analytical Methods in*
919 *Geomechanics* 32, 1365–1383.
- 920 Richefeu, V., El Youssoufi, M.S., Radjai, F., 2006. Shear strength properties
921 of wet granular materials. *Physical Review E* 73, 051304.
- 922 Russell, A., Khalili, N., 2006. A unified bounding surface plasticity model
923 for unsaturated soils. *International Journal for Numerical and Analytical*
924 *Methods in Geomechanics* 30, 181–212.
- 925 Scholtes, L., Chareyre, B., Nicot, F., Darve, F., 2009. Micromechanics of
926 granular materials with capillary effects. *International journal of engineer-*
927 *ing science* 47, 64–75.
- 928 Scholtès, L., Hicher, P.Y., Nicot, F., Chareyre, B., Darve, F., 2009. On the
929 capillary stress tensor in wet granular materials. *International journal for*
930 *numerical and analytical methods in geomechanics* 33, 1289–1313.
- 931 Sheng, D., 2011. Review of fundamental principles in modelling unsaturated
932 soil behaviour. *Computers and Geotechnics* 38, 757–776.

- 933 Šmilauer, V., Catalano, E., Chareyre, B., Dorofeenko, S., Duriez, J., Gladky,
934 A., Kozicki, J., Modenese, C., Scholtès, L., Sibille, L., et al., 2021. Yade
935 reference documentation. Yade Documentation 3rd ed. URL: [http://](http://yadedem.org/doc/)
936 yadedem.org/doc/.
- 937 Soulie, F., El Youssoufi, M.S., Cherblanc, F., Saix, C., 2006. Capillary co-
938hesion and mechanical strength of polydisperse granular materials. The
939 European Physical Journal E 21, 349–357.
- 940 Sun, Y., Beckermann, C., 2007. Sharp interface tracking using the phase-field
941 equation. Journal of Computational Physics 220, 626–653.
- 942 Van Genuchten, M.T., 1980. A closed-form equation for predicting the hy-
943draulic conductivity of unsaturated soils. Soil science society of America
944 journal 44, 892–898.
- 945 Vlahinić, I., Jennings, H.M., Andrade, J.E., Thomas, J.J., 2011. A novel and
946 general form of effective stress in a partially saturated porous material: The
947 influence of microstructure. Mechanics of Materials 43, 25–35.
- 948 Wan, R., Duriez, J., Darve, F., 2015. A tensorial description of stresses in
949 triphasic granular materials with interfaces. Geomechanics for Energy and
950 the Environment 4, 73–87.
- 951 Wan, R., Pouragha, M., Eghbalian, M., Duriez, J., Wong, T., 2019. A
952 probabilistic approach for computing water retention of particulate systems
953 from statistics of grain size and tessellated pore network. International
954 Journal for Numerical and Analytical Methods in Geomechanics 43, 956–
955 973.

- 956 Wang, J.P., Gallo, E., François, B., Gabrieli, F., Lambert, P., 2017. Capillary
957 force and rupture of funicular liquid bridges between three spherical bodies.
958 Powder Technology 305, 89–98.
- 959 Weber, J., 1966. Recherches concernant les contraintes intergranulaires dans
960 les milieux pulvérulents. Bulletin de liaison des Ponts et Chaussées 20,
961 1–20.
- 962 Yang, G., Jing, L., Kwok, C., Sobral, Y., 2019. A comprehensive parametric
963 study of lbm-dem for immersed granular flows. Computers and Geotechnics
964 114, 103100.
- 965 Younes, N., Benseghier, Z., Millet, O., Wautier, A., Nicot, F., Wan, R., 2022.
966 Phase-field lattice boltzmann model for liquid bridges and coalescence in
967 wet granular media. Powder Technology , 117942.
- 968 Yuan, C., Chareyre, B., 2022. Transitioning from the funicular to the pen-
969 dular regime in granular soils. Géotechnique 72, 825–831.
- 970 Yuan, C., Chareyre, B., Darve, F., 2018. Deformation and stresses upon
971 drainage of an idealized granular material. Acta Geotechnica 13, 961–972.